Hollow Fiber Coupler Sensor

by

Nithin S. Kuruba
BE, Visvesvaraya Technological University, 2012

A Thesis Submitted in Partial Fulfillment of the
Requirements for the Degree of

MASTER OF APPLIED SCIENCE

in the Department of Electrical and Computer Engineering

Hollow Fiber Coupler Sensor

by

Nithin S. Kuruba
BE, Visvesvaraya Technological University, 2012

Supervisory Committee

Dr. Tao Lu, Supervisor
(Department of Electrical and Computer Engineering)

Dr. Poman P. M. So, Departmental Member
(Department of Electrical and Computer Engineering)

Supervisory Committee

Dr. Tao Lu, Supervisor
(Department of Electrical and Computer Engineering)

Dr. Poman P. M. So, Departmental Member
(Department of Electrical and Computer Engineering)

ABSTRACT

This thesis presents a method to fabricate a robust optical directional coupler sensor using a solid core fiber (SCF) and a hollow core fiber (HCF). Through evanescent wave coupling mechanism, the optical power is exchanged between SCF and HCF. The hollow core of the HCF can be filled with liquid samples to alter the coupling ratio which imparts change in amount of light propagating through the SCF. Thus, it gives the coupler with ability of sensing refractive index of the sample with good sensitivity of 4.03 ± 0.50 volts per refractive index units (V/RIU) for refractive indices ranging from 1.331 ± 0.003 to 1.403 ± 0.003 with a resolution of 3.5×10^{-3} refractive index units (RIU). The SCF-HCF coupler was also used to sense the temperature based on the concept of temperature dependence on refractive index of the sample inside the hollow core of HCF. Further, the packaging methods are described that protect coupler from ambient environments and improves the life span of sensor.

Contents

List of Tables

List of Figures

ACKNOWLEDGEMENTS

I would like to thank:

Dr. Tao Lu for his valuable guidance, constant support and passion in research to motivate and encourage me as my supervisor through out my degree. His patience and flexibility helped me to work on my studies and thesis in a productive and independent manner;

Dr. Elaine Humphrey for the help on the advanced microscopy facilities.

CONTRIBUTION

T.L. conceived and designed the experiments; N.K. performed the experiments and modelling; N.K. and T.L. analyzed the data; N.K. wrote the report.

DEDICATION

I dedicate this thesis to my parents, who have been my pillars of support throughout all phases of my life.

Chapter 1

Introduction

1.1 Sensors

Sensors play crucial role in modern life. They improve quality, reliability and accuracy of the measurement systems that support healthy living of a human being. They can capture physical parameters of a biological species or the concentration of biochemical species.

A sensor acts on wide variety of measurands, such as humidity[2], temperature, pressure[3], chemical composition[4], acceleration and pH and generates relevant output in form of analog signal that can be used for various data extraction purposes by implementing different data processing schemes. A sensor ideally transduces one quantity to another, which is human readable form.

There has been an immense development in the field of sensors and it is getting better everyday. The research in the field of sensors has been of great interest for many researchers and students. To build a sensor, it is required to understand and model the physical phenomena and based on which the sensing mechanism can be built.

1.2 Optical fibers

Optical fibers bought the evolution in the field of sensors and they have been extensively used in research. There are many companies that supply fiber optic components and other devices required for research and this has been an encouraging factor for further research and it leads to development of fiber optic industries. They have numerous applications in medical[5, 15], environmental, telecommunications communications [8] and pharmaceutical[6] fields as well.

Optical fibers, due to their excellent light guiding and data transmission capabilities, they stand favorites in building sensors. They offer high flexibility, easily multiplexible [7, 9] and good sensitivity over the existing systems. Some of the other advantages using optical fibers include low cost, small size [10], robustness and ability to be used in unfavorable conditions such as noise, electromagnetic fields [11], high voltages, nuclear radiation and explosive or chemical corrosive media [12]. Their applications to humidity and moisture sensing are reported[13]. As per [14], optical fibers find applications in health monitoring and high speed railway monitoring as well. Due to smaller sizes of the optical fiber sensors, they make way for surface mounting or can be enclosed under different materials.

Due to the growing demand for optical fibers in transducer and communications technology, many applications are being developed using wide number of optical sensors built from the basic optical fibers. These sensors are lightweight, fast, stable and small in size, due to which they are getting recognition in the field of aerospace and bio-medical industry[15].

1.3 Refractive Index Sensors

Refractive index (RI) measurement is one of the key aspect for sensors as identifying the right refractive index can label the samples and can measure purity of it [16]. Refractive index varies on factors such as material composition, temperature, pressure and stress. Refractive index can be defined as ratio of speed of light in vacuum and its velocity in the medium. As the refractive index value of a material increases, the speed of the light drops, i.e. they are inversely proportional to each other.

$n = c/v$, where c is the speed of light and v is the velocity.

The introduction of various refractometric techniques has spawned an evolution in refractive index sensing. As it plays a key role in many biological, chemical and environmental applications. Refractive index (RI) of substrate can be found by refractometers and there are four main types of refractometers, including traditional handheld refractometers, digital handheld refractometers, Abbe refractometers and inline process refractometers [16]. Basically refractive index sensors measure refractive index and based on which they are used for detecting many chemical substances. There are other applications that are associated with measuring of refractive index and few among them are detecting salinity of water [17], adulteration of chemical liquids, determination of sugars [18], protein concentration [19] [20], air pressure sensing [21] and environmental pollution.

In modern applications, there is a high demand for miniaturization, real time and in-situ sensing. Therefore, optical fiber based refractive index sensors are gaining much popularity. Also they are portable and maintenance free when compared to conventional refractometric devices.

1.3.1 Performance of RI Sensors

There are many refractive index sensors in market and they work on different principles. However, it is mandatory to evaluate the performance of these sensors to judge if they are effective and reliable. Evaluating the performance will give flexibility to the end user in comparing different sensors with ease. The performance of RI sensors can be evaluated based on few parameters such as sensitivity, resolution and limit of detection (LOD). They are defined as:

- Sensitivity: The sensitivity is a ratio of the incremental change in the output of sensor (Δy) to the incremental change of the measurand in input (Δx) [22]. Sensitivity is a main parameter that determines the performance of refractive index sensor. The sensitivity of our refractive index sensor can be measured as the ratio of change of output voltage due to change of refractive index of the measurand, such that (Δy) is the change in transmission and (Δx) is the change in the refractive index of measurand.

An ideal sensor will have large and constant sensitivity in its operating range. However, the sensitivity alone cannot evaluate sensor performance quantitatively. The sensitivity together with resolution and limit of detection shall help analyze the performance of RI sensor effectively.

- Resolution: The resolution is another parameter which gives information about how well the sensor detects the smallest change in the input. Resolution can also be defined as the minimal change of measurand that can generate an identifiable change in the output. The resolution can be calculated as,

  $$\frac{V_n}{S}[23]$$

  where V_n is the standard deviation or noise and S is the sensitivity. The resolution is related to precision with which measurement is made but is not same as precision. In case of high noise, the resolution value can be highly dented.

- LOD: LOD can be defined as the lowest concentration of the analyte in a sample that can induce an observable signal under stated conditions of a test [24]. There is common method to detect the LOD, i.e. by using the standard deviation of the blank and sensitivity.

  In case of a linear relationship ($y = m \times x + b$) between the response y and the limited range of concentration x, the LOD can be calculated as:

  $$LOD = 3 \times S_a/m; \tag{1.1}$$

  where S_a is the standard deviation of the response from y-intercepts/residuals and m is the slope obtained from the linear regression model.

1.3.2 Review of Refractive index sensors

Since advancement of optical fiber technology, there has been wide number of developments in building optical fiber based refractive index sensors. These sensors measure the refractive index based on different optical fiber configurations and techniques. Some of them are based on Surface Plasmon Resonance (SPR) [31, 30, 29], Fiber Bragg Grating(FBG) [43, 41, 42, 38], Long Period Grating (LPG)[48, 25, 51, 26] and

Fiber Coupling [44, 27, 54, 61] techniques. In this report, we provide an overview of these sensors and their configurations. We also discuss about the pros and cons pertaining to these sensors and finally list the performance parameters at the end of each section for comparing purposes.

SPR

A surface plasmon is a charge density that occurs at the interface of two media such as metal and dielectric. It can be excited by light, i.e. when light incidents on the metal-dielectric interface at a certain angle. The energy from incident light is then transferred to the surface plasmons reducing the intensity of the reflected light. This creates a sharp dip in the reflected light that can be captured[28].

Surface plasmons are basically transverse magnetic waves that propagate along the interface between the metal and dielectric. Since they travel in the vicinity of the metal layer, any changes in the refractive index of the media near the metal layer can induce variations in the propagation of the surface plasmons. such variations can be recorded by monitoring the interactions of surface plasmon and optical light wave, creating a platform for sensing applications. Also the adsorption property of the metal makes it possible to develop surface plasmon based sensors [31, 30, 29]. SPR based sensors have been proposed using different configurations, such as using LPG[30] and regular waveguides[29, 31] as the dielectric material.

SPR based sensors utilizing gratings operate on principle of exciting long range surface plasmon mode of a metal coated waveguide with a long period grating etched on the core. Such that the mode is excited at specific wavelength and serves as the measure of refractive index of the external medium. SPR based sensors configurations that use regular optical fiber as a dielectric layer work on a principle of exciting surface plasmons at the interface of metal layer, such that these excited surface plasmons respond to changes in the refractive index in the surrounding media of metal and thus causes a shift in resonance angle or resonance wavelength depending upon the respective type of interrogation. Since SPR based waveguide sensors are built using optical fibers, different fiber optic configurations can be used as part of sensor design, such as D-shaped, polished and tapered optical fibers [32]. SPR based sensors offer benefits such as small in size, good sensitivity and flexibility. They also incorpo-

rate advantages offered by optical fibers. However, as per [33] SPR sensors exhibit an inherent limitation, that is the refractive index measurements may be compromised by the interfering effects. The effects such as adsorption of non target molecules by sensor surface and background refractive index variations caused by measurand temperature and composition fluctuations, which can add variations in the measured refractive index measurements.

Table 1.1: Surface plasmon based refractive index sensors and their performance parameters.

Reference	**RI Range**	**Sensitivity**	**Resolution**	**Year**
[31]	1.405 - 1.42	2,000 dB/RIU	2×10^{-5}	1997
[30]	1.5090 - 1.5110	$-4.9 \times 10^{4} nm/RIU$	-	2009
[29]	1.5375 - 1.5515	$\sim 45 \mu M/RIU$	-	2016

FBG

FBG's are small fiber optic components. "They contain a periodic perturbation of the refractive index along the fiber length which is formed by exposure of the core to an intense optical interference pattern" [34]. FBG technology is one among the popular techniques used for developing sensors for measurement of various physical, chemical parameters. FBG sensors operate as per the principle stated in [35], when light is passed through FBG, a part of light with specific wavelength is reflected back due to periodic refractive index variations. This wavelength is known as bragg wavelength (BW). BW is sensitive to any variations in the fiber optic properties caused by surrounding temperature or pressure etc. and thus any shift of this wavelength can be analyzed to provide the information about the surrounding environment.

Since FBG is protected by cladding, when the FBG sensor is immersed in different environments, the BW of light traveling through core remains unaffected. So in order to expose the fiber optic core to the surrounding environment, the cladding is etched and thus the traveling modes in the fiber core becomes vulnerable to the changes in the surrounding environment, such as refractive index. Therefore, when FBG refractive index sensor is immersed in a liquid sample, the respective BW undergoes a shift due to change of refractive index of the surrounding media of the sensor

[36, 37]. By analyzing this wavelength shift, the refractive index of the liquid sample under test can be discerned.

There are some of the methods which are presented to reduce the cladding material around the optical fiber to expose the evanescent field to the surrounding medium and two such methods are D-shaped Method[38, 39, 43] and Chemical etching[40, 41]. [42] presented a different technique, in which a etch-eroded fiber Fabry-Prot interferometer (FFPI) is built using two FBG's, claiming to provide narrower resonance spectral feature and higher sensitivity than a regular FBG based sensors.

Even though FBG based refractive index sensors offer advantages such as good resolution and sensitivity capabilities, they require high cost and special protective and reliable packaging to protect the core of optical fiber. Also the fabrication process of these sensors include complexities and they offer limited lifespan [46].

Table 1.2: Fiber bragg grating refractive index sensors based on spectral shift measurement method and their performance parameters.

Reference	**RI Range**	**Sensitivity**	**Resolution**	**Year**
[43]	1.326 - 1.333	-	5×10^{-5}	1996
[41]	1.33 - 1.42	4.6×10^{-6}	-	1997
[42]	1.000 - 1.378	$71.2nm/RIU$	1.4×10^{-4}	2005
[38]	1.33 - 1.44	$0.02nm/RIU$	-	2016

LPG

LPG is a type of FBG but with periodic modulations of refractive index in fiber optic core and the periodicity range in between "few hundreds of a micron" [47]. Basically, a guided mode propagating in the core is perturbed due to the refractive index perturbations and as it propagates, it couples with one of the cladding modes when their propagation constants match at a particular wavelength. Then the coupled modes get lost due to absorption and scattering nature of the cladding. The effective refractive indices of the cladding modes are sensitive to the fluctuations in the surrounding environment. When the refractive index of the media in the vicinity of cladding modes is

increased, the propagation constant of the cladding mode become complex and thus are lost. i.e. the change in the refractive index of the surrounding media can modify the period of LPG, thus impacting the phase matching conditions for coupling to the cladding modes and introducing a change in position of the resonance wavelength in the output spectrum[45]. By analyzing the wavelength shift quantitatively, the refractive index of the sample under test can be identified.

Several papers are published reporting refractive index sensing by LPG's[48, 47]. Different ways are suggested to improve the sensitivity and among them one way was by using overlays [25, 49], in which the transmission spectrum wavelengths depend on the optical thickness of the overlay material and the other way to improve the sensitivity was by using fibers other than regular ones for building gratings such as pure silica core fiber [50] and PCF[51, 26]. The sensor demonstrated by [26] offered a detection limit of 2×10^{-5}.

LPG refractive index sensors have advantages and limitations. As part of advantages, since they are made from optical fibers, they can be mass produced in less time, small in size, can be integrated with other optical devices with ease and offers good sensitivity and resolution. Also they posses all the advantages that are associated with optical fibers. Some of the drawbacks using LPG based refractive index sensors are that they are bend sensitive and vulnerable to fluctuations of the other parameters such as strain, temperature etc. while refractive index being the only parameter that's being monitored. The other drawback is that they require packaging to protect the core and cladding materials from the surrounding environment and simultaneously maintain the higher sensitivity. The packaging process shall increase the life span of the sensor and thus making it a reusable sensing device.

Table 1.3: Long period grating refractive index sensors based on spectral shift measurement method and their performance parameters.

Reference	**RI Range**	**Sensitivity**	**Resolution**	**Year**
[48]	1.404 -1.452	-	7.69×10^{-5}	1996
[50]	1.3211-1.3271	40 nm/RIU	-	2006
[26]	1.33	1,500 nm/RIU	-	2007
[51]	1.3333-1.3792	2,343 nm/RIU	8.5×10^{-6}	2016

Couplers

Couplers are fiber optic devices made from optical fibers, which are used extensively in the field of optics. They are used in splitting signals or to combine them. The functional and fabrication details of directional couplers are discussed in detail in the next section. In this section, we will discuss about coupler based refractive index sensors and their configurations.

Couplers are generally fabricated through tapering both the fibers together, due to which the cladding of both the fibers at the junction shrinks and the evanescent field generated is exposed to the surrounding environment. Any changes in parameters such as temperature, pressure, strain etc. can affect the transmission spectrum of the fiber optic coupler.

Directional coupler based refractive index sensors built using regular optical fibers have been proposed. The coupler based refractive index sensor presented in [44] has two identical fibers that shows the sinusoidal transmission spectrum. When a ligand is dropped on the surface of the coupler junction, the evanescent field is affected by the refractive index change in the surrounding media and thus creates a shift in the transmission spectrum. The sensor was used to detect refractive index changes in samples of water-ethanol and it was also used in detection of avidin by immobilizing biotin on the surface of the coupler.

[61] presented a coupler fabricated using regular single mode fiber and home-made hollow fiber, such that the hollow fiber could be filled with different samples. The variation in refractive index of the sample inside hollow fiber tunes the guiding properties of light propagating in single mode fiber and thus allowing the sensor to be used as a RI sensor. The sensor was used to detect the refractive index variations in samples of Fe_3O_4 - glycerol.

There are other coupler based refractive index sensors that make use of different sensor configuration in terms of type of fiber used, such as photonic crystal fiber(PCF)[54, 27]. A PCF is a specialty fiber with an internal periodic capillaries, filled with air, that are arranged in a hexagonal lattice. PCF's are made in such a way that, one of the capillary in the center is replaced with a core structure to guide the light. These fibers exhibit properties of both optical fibers and photonic crystals

[52].

A coupler structure employing a PCF was presented in [54], in which directional coupler architecture was embedded within a PCF such that the modes of hollow and solid cores get coupled, thus giving PCF the ability to act as a directional coupler. The refractive index of sample is varied through temperature and due to which it produces a shift in the resonance wavelength and by analyzing the spectrum data, the sample under investigation can be discerned. The sensor offered a minimal detection limit of $6.66 \times 10^{-8} RIU$. The sensor presented by [27] also employs coupler configuration in a PCF and the detection limit offered by the sensor was 4.6×10^{-7}.

The below table represents the parameters of the sensors discussed in this section.

Table 1.4: Coupler based refractive index sensors and their performance parameters.

Reference	**Detection Limit**	**Sensitivity**	**Resolution**	**Year**
[44]	-	4×10^{-6}	-	2005
[27]	4.6×10^{-7}	30,100 nm/RIU	8.5×10^{-6}	2009
[54]	$6.66 \times 10^{-8} RIU$	15,600 nm/RIU	-	2013
[61]	-	73,000 nm/RIU	-	2016

1.4 Hollow Core Fiber (HCF)

Recently, HCFs have been proved to be low cost, highly sensitive and feasible solutions for refractive index sensing and based on which some of the techniques have been outlined which employed HCFs such as hollow core Bragg fiber (HCBFs) [53, 55] and Photonic crystal fiber (PCF) [56]. HCFs have been used not only for sensing refractive index but also used as a pressure sensor [57]. Due to their excellent geometrical structure, it makes them suitable for temperature sensing applications and few of them are developed by [58, 59, 60].

Hollow fiber has a hollow core and a solid cladding. The hollow core is specifically designed for filling it with different samples as part of sensing application. Fused silica capillary tubing is one such type of hollow fiber, its construction involves

a hollow silica tube coated with a polymer on the outer surface as shown in the Fig. 1.1.

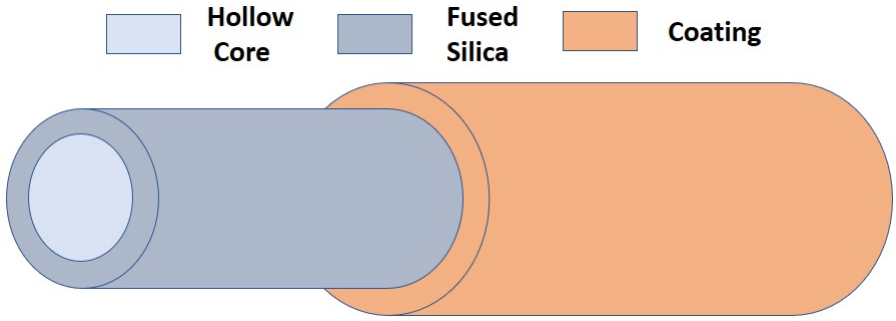

Figure 1.1: Hollow fiber with fused silica layer and polyimide coating.

The coating on the silica layer of the fiber protects the waveguide from high abrasion. The composition of the coating can be modified, such that the hollow wave guide can be used as a liquid conduit and as a light guiding fiber.

If a sample is passed into the hollow core of HCF, any molecules present in the sample interact with light entering the hollow core and thus creates a platform for analyzing the sample under investigation.

1.5 Directional coupler

Optical directional couplers are optical devices which can combine or divide the light energies. They are also used as the beam amplifiers, which combine light from different sources and provides amplified standalone output. These devices generally have four ports formed from two individual wave guides and make up a 2x2 directional coupler. It receives input at one of the input port and performs distributed coupling among the wave guides, which results in the power transfer between the waveguides. These couplers posses the ability to transfer the light between the adjacent fibers, which makes them suitable for building sensors.

Directional couplers are not limited to two inputs and two outputs but can be extended to $n \times m$ inputs and outputs, where n is the number of inputs and m is the number of outputs and n, m numbers are chosen based on the intended type of application of the coupler. Directional couplers can either be active or passive

components. Active fiber couplers make use of other optical devices such as splitters, photorecievers etc. and transmit the light. Where as the passive fiber couplers simply propagate the light energy.

The evanescent field in these optical directional couplers flow the power between the fibers. This field is bound to an EM wave of the mode propagating through the fiber and it penetrates through the cladding of the other fiber and propagates through the core region. These devices can be used as directional coupler sensors [62]. There are other advanced applications developed such as mode selective coupler [63], coupling between single mode and photonic crystal fiber [64] [65] and broadband coupler [66].

OFCs are generally fabricated using tapering method and same method can be applied to build a SCF-HCF coupler. One such coupler was developed for detecting magnetic fluid strength and it's concentration by [61]

1.6 Objective

In this thesis, we used our fabricated coupler[1] to sense the refractive index and consequently temperature of liquid sample flowing inside the core of HCF. This was possible because the amount of light evanescently coupled from the SCF to HCF and back to SCF depends on sensitivity of the refractive index of the flowing liquid. Meanwhile the temperature change of the liquid inside core of HCF changes its refractive index, and consequently the amount of light transmitted back to SCF.

1.7 Thesis Outline

This thesis focuses mainly on the fabrication of a SCF-HCF directional coupler which acts as a refractive index and temperature sensor.

Chapter 2 provides basic theory of evanescent wave sensors, obtaining an expression to describe evanescent wave and principle of coupling behind fabrication of SCF-HCF coupler.

Chapter 3 illustrates a graphical representation of power coupling across the wave guides. The simulation was developed under wave optics module of comsol .

Chapter 4 describes various coating removal methods, fiber cleaving methods and coupler fabrication methods. The method opted to fabricate the SCF-HCF coupler.

Chapter 5 presents the experimental setup and optical components included in the setup to carry forward the experiment. It also discusses about experimental results, device sensitivity and resolution. Further, coupler packaging methods have been discussed.

Chapter 6 concludes the thesis and discusses about possible future work to improvise the device.

Chapter 2

Background Theory

Intensity modulated sensors are type of fiber optic sensors that work on the principle of change in amount of light intensity within the optical fiber [67, 68]. Whenever a light propagating through an optical fiber encounters a measurand or a foreign sample, it undergoes a change and the light intensity recorded will be different from that of the source. By analyzing the resultant output intensity, the properties of the measurand can be estimated.

Intensity modulated sensors depend upon optical properties of the measurand. They offer advantages such as ease of fabrication, robustness, and simplicity of signal processing [67]. Frustrated total internal reflection (FTIR) based sensor is one type of intensity modulated sensor. It works on the principle of evanescent field created by total internal reflection. In the next section, we discuss about the fundamental concepts of total internal reflection and evanescent wave.

2.1 Evanescent Wave

2.1.1 Light propagation inside the fiber

Light is an electromagnetic wave similar to a radio wave but with much higher frequency. When light from a source is directed to hit a surface, then the angle at which

it strikes the surface is known as the angle of incidence and the angle at which it reflects from the surface is known as the angle of reflection. The angle of incidence will be equal to angle of reflection. If the same light traverses into a different medium from the surface, it bends and this phenomena is called as refraction.

Consider a light ray traveling through a medium of higher refractive index (n_1) hits the interface at an angle of incidence (θ_i), then some part of light is partially transmitted through the second medium of lower refractive index (n_2) at angle of refraction θ_t and the ray is called as transmitted ray. The remaining part of light reflects back from the interface at an angle of reflection θ_r and is called as reflected ray. The same has been graphically represented in Fig. 2.1.

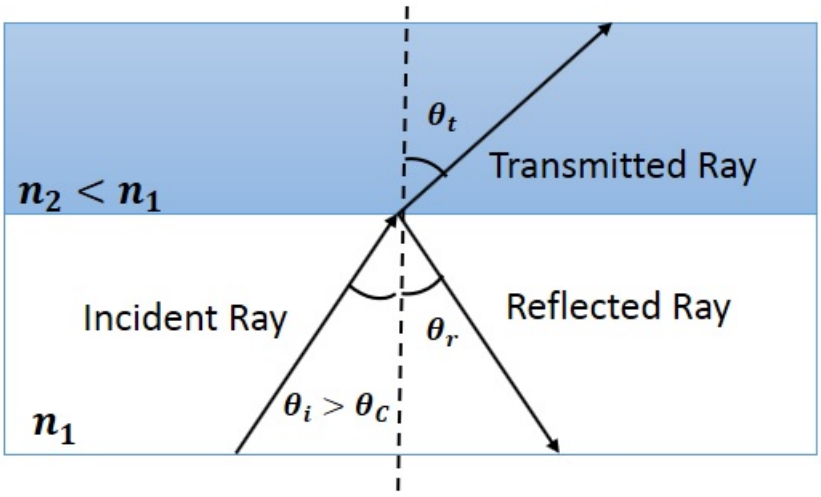

Figure 2.1: Reflection and refraction of a plane wave at a plane interface.

According to the Snell's law, the angle of incidence θ_i and refraction θ_t are related to each other and to the higher refractive index medium n_1 and lower refractive index medium n_2 as:

$$n_1 sin\theta_{\mathrm{i}} = n_2 sin\theta_{\mathrm{t}} \tag{2.1}$$

As shown in Fig. 2.1, a light ray travelling through the media of refractive index n_1 hits the interface of two different media at an angle of incidence θ_i. At a certain angle of incidence, angle of refraction is 90° and due to which the incident light beam traverses parallel to the interface between the dielectrics (n_1, n_2). The angle of incidence at which this condition satisfies is called as critical angle and it is given as:

$$\theta_{\mathrm{c}} = sin^{-1}\left(\frac{n_2}{n_1}\right) \tag{2.2}$$

The critical angle is the largest angle of incidence at which the refraction can still occur. If the angle of incidence is greater than the critical angle (θ_c), then the incident light beam undergoes total internal reflection at interface of n_1 and n_2. If the angle of incident light beam is less than the critical angle, it undergoes refraction and leaks into lower refractive index region(n_2) and will be lost.

Snells's law applies to optical fibers as well. The core of an optical fiber has higher refractive index (n_1) than that of cladding (n_2), so the light incident into an optical fiber at an angle greater than the critical angle travels in a zig-zag fashion causing total internal reflections and thus propagates through the fiber core. In all the reflections inside the fiber core, as long as propagating rays satisfy $\theta_i > \theta_c$ remain confined to the core of the fiber.

In ideal condition the complete light should propagate inside core of optical fiber, but if we refer to electromagnetic theory of light, it says that during total internal reflection, some part of light intensity inside the cladding region of an optical fiber exists and it is of decaying in nature as shown in Fig. 2.2. This field is known as an evanescent field or wave.

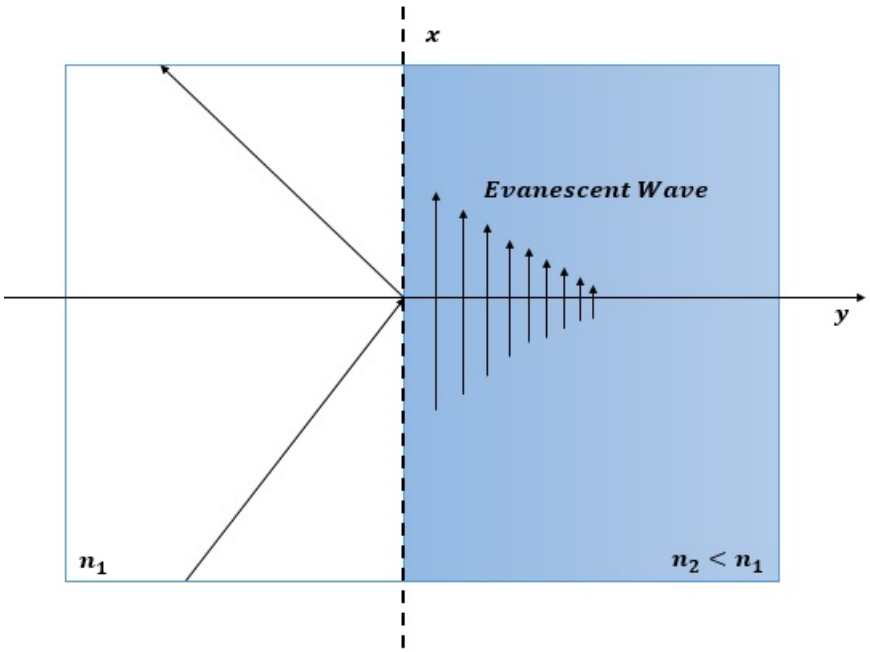

Figure 2.2: The arrows representing the amplitude of electric field decaying along the direction of y describing an evanescent wave.

The penetration depth of the evanescent wave can be estimated as per [69].

The evanescent field I decays exponentially with distance z from the interface according to $I(z) = I(0) \times e^{-z/d}$, given that $I(0)$ is the intensity at the interface and penetration depth is given by,

$$d = \frac{\lambda}{4\pi}[n_1^2 sin^2(\theta_i) - n_2^2]^{-1/2} \tag{2.3}$$

where λ is the wavelength of the light, n_1 and n_2 are the refractive indices of medium 1 and 2 and θ_i is the angle of incidence.

2.2 Directional Coupler

The two main concepts behind functioning of our hollow coupler sensor are light guiding through the fibers, achieved through total internal reflection as mentioned in the previous section and power coupling between SCF and HCF.

As discussed in earlier section, optical fibers consist of a core of higher refractive index and a cladding of lower refractive index. Light rays enter the fiber core at range of angles and they keep propagating inside the core as long as they are hitting the core-cladding interface at angles greater than critical angle. These rays are called as modes, which is typically the case in multimode fibers as there exists many modes. If the core diameter is small enough, then the number of possibly totally internally reflected rays reduce to one and thus giving rise to one single mode traveling through optical fiber core. As the mode propagates, the tail of the evanescent wave expands to the cladding region.

To accurately describe the propagation of light inside an optical wave guide, a rigorous model known as the wave model can be used and in which the light is treated as an electromagnetic wave. In this model, the propagation of light in an optical fiber is characterized by a set of guided electromagnetic waves called modes. Every guided mode is an pattern of electric or magnetic distribution repeated along the equal intervals and are governed by Maxwell's equations. Modes can be defined by the properties of coherence and orthogonality: Orthogonal solutions of wave equation those do not interfere[70].

2.2.1 Modal Analysis

Maxwell's equations are the starting point for the modal analysis. We consider Maxwell's equations for isotropic, linear, non conducting and non magnetic medium as per [72].

$$\nabla \times \vec{E}(x,y,z,t) = -\frac{\partial \vec{B}}{\partial t}(x,y,z,t) \tag{2.4}$$

$$\nabla \times \vec{H}(x,y,z,t) = \frac{\partial \vec{D}}{\partial t}(x,y,z,t) \tag{2.5}$$

$$\nabla \cdot \vec{D}(x,y,z,t) = 0 \tag{2.6}$$

$$\nabla \cdot \vec{B}(x,y,z,t) = 0 \tag{2.7}$$

Given that $\vec{B}(x,y,z,t) = \mu\vec{H}(x,y,z,t)$ and $\vec{D}(x,y,z,t) = \epsilon\vec{E}(x,y,z,t)$, in which ϵ and μ denote permittivity and permeability of the medium. They are related to respective values in vaccum of $\epsilon_0 = 8.854 \times 10^{-12}[F/m]$ and $\mu_0 = 4\pi \times 10^{-7}[H/m]$ by $\epsilon = \epsilon_0 n^2$ and $\mu = \mu_0$, where n is the refractive index of the medium [73]. Also, $\vec{E}(x,y,z,t)$ is electric field, $\vec{H}(x,y,z,t)$ is magnetic field, $\vec{B}(x,y,z,t)$ is magnetic flux density and $\vec{D}(x,y,z,t)$ is the electric displacement vector.

In this report, we make use of expressions derived in [71] to describe the modes in optical fibers.

By assuming electromagnetic fields are monochromatic functions of time that oscillate at a single angular frequency ω, we can write phasor form of electric field $\vec{E}(x,y,z,t)$, magnetic field $\vec{H}(x,y,z,t)$, electric flux density $\vec{D}(x,y,z,t)$ and magnetic flux density $\vec{B}(x,y,z,t)$ as:

$$\vec{E}(x,y,z,t) = Re(\vec{E}(x,y,z)exp(j\omega t)), \tag{2.8}$$

$$\vec{H}(x,y,z,t) = Re(\vec{H}(x,y,z)exp(j\omega t)), \tag{2.9}$$

$$\vec{D}(x,y,z,t) = Re(\vec{D}(x,y,z)exp(j\omega t)), \tag{2.10}$$

$$\vec{B}(x,y,z,t) = Re(\vec{B}(x,y,z)exp(j\omega t)) \tag{2.11}$$

In following sections for convenience purposes we refer $\vec{E}$ as $\vec{E}(x, y, z)$ unless otherwise specified. We also adopt similar simplification to refer $\vec{H}$ as $\vec{H}(x, y, z)$, $\vec{B}$ as $\vec{B}(x, y, z)$ and $\vec{D}$ as $\vec{D}(x, y, z)$.

Using all these considerations, we can write the time harmonic Maxwell's equations for linear, isotropic, non-conducting and non-magnetic medium in terms of phasor form as given below.

$$\nabla \times \vec{E} = -j\omega\vec{B} \tag{2.12}$$

$$\nabla \times \vec{H} = j\omega\vec{D} \tag{2.13}$$

$$\nabla \cdot \vec{D} = 0 \tag{2.14}$$

$$\nabla \cdot \vec{B} = 0 \tag{2.15}$$

where $\vec{D} = \epsilon\vec{E}$, $\vec{B} = \mu\vec{H}$ and $\epsilon = \epsilon_0\epsilon_r$, $\mu = \mu_0\mu_r$ in which μ_0 and ϵ_0 are the permeability and permittivity of vaccum, whereas μ_r and ϵ_r are the relative permeability and relative permittivity of the material. Since the source domain is non-magnetic, we can assume $\mu_r = 1$.

By applying curl operator for the equation 2.13, we get:

$$\nabla \times (\nabla \times \vec{E}) = -j\omega\nabla \times \vec{B} \tag{2.16}$$

we can expand left hand side of equation 2.16 to:

$$\nabla \times (\nabla \times \vec{E}) = \nabla(\nabla \cdot \vec{E}) - \nabla^2\vec{E} \tag{2.17}$$

in which ∇^2 is a Laplacian operator defined as:

$$\nabla^2 = \frac{\partial^2}{\partial x^2} + \frac{\partial^2}{\partial y^2} + \frac{\partial^2}{\partial z^2} \tag{2.18}$$

The equation 2.15 can be written as:

$$\nabla \cdot \vec{D} = \nabla \cdot (\epsilon_0\epsilon_r\vec{E}) \tag{2.19}$$

and it can be re-written as:

$$\epsilon_0\nabla \cdot (\epsilon_r\vec{E}) = \epsilon_0(\nabla\epsilon_r \cdot \vec{E} + \epsilon_r\nabla \cdot \vec{E}) = 0 \tag{2.20}$$

and we obtain:

$$\nabla \cdot \vec{E} = -\frac{\nabla \epsilon_r}{\epsilon_r} \cdot \vec{E} = 0 \tag{2.21}$$

Using equations 2.19 and 2.21, we can re-write LHS and RHS expression of equation 2.16 as:

$$-\nabla(\frac{\nabla \epsilon_r}{\epsilon_r} \cdot \vec{E}) - \nabla^2 \vec{E} = k_0^2 \epsilon_r \vec{E}$$

where k_0 is the wave number of vaccum and it is given as:

$$k_0 = \omega\sqrt{\epsilon_0 \mu_0} = \frac{\omega}{c} \tag{2.22}$$

Thus, the wave equation of electric field for a medium with relative permittivity ϵ_r as per [71] is given as:

$$\nabla^2 \vec{E} + \nabla(\frac{\nabla \epsilon_r}{\epsilon_r} \cdot \vec{E}) + k_0^2 \epsilon_r \vec{E} = 0 \tag{2.23}$$

The wave number k in the medium is given as:

$$k = k_0\, n$$

But if the relative permittivity ϵ_r is piecewise homogeneous, the above given vectorial wave equation can be reduced to Helmholtz equation as given below.

$$\nabla^2 \vec{E} + k^2 \vec{E} = 0 \tag{2.24}$$

Similarly, we can derive Helmholtz eqution for magnetic field as shown below.

$$\nabla^2 \vec{H} + k^2 \vec{H} = 0 \tag{2.25}$$

$\vec{E}$ and $\vec{H}$ in above given Helmholtz equations are the functions of three space coordinates and k is a wave number.

As per the definition of our SCF and HCF, the wave propagates in z direction and is independent of refractive index variations in transverse coordinates x and y. As an example, electric field phasor can be represented as given below.

$$\vec{E} = \vec{E}(x, y)e^{-j\beta z} \tag{2.26}$$

We use separation of variables method to separate z coordinate from the transverse coordinates and make substitutions, such that $\frac{\partial}{\partial z} \rightarrow -j\beta$. Using this method, the three dimensional Laplacian operator ∇^2 from the Helmholtz equations 2.24 and 2.25 is separated into two parts. The first part is $\nabla_\perp$ for the cross sectional coordinates x,y that represent the transverse part, which is the variation of refractive index $n^2(x, y)$ and the second part is ∇_z, which represents the longitudinal coordinate.

$$\nabla^2 \vec{E} = \left(\nabla_\perp^2 + \frac{\partial^2}{\partial z^2}\right)\vec{E} \tag{2.27}$$

$$= \left(\nabla_\perp^2 - \beta^2\right)\vec{E}(x, y) \tag{2.28}$$

In the above equation, the transverse part of Laplacian operator $\nabla_\perp^2$ is replaced by the cartesian version of $\nabla_\perp^2 = \frac{\partial^2}{\partial x^2} + \frac{\partial^2}{\partial y^2}$. The waveguides used to build SCF-HCF sensor have cylindrical geometry, so we can consider cylindrical coordinates to represent the first part of Laplacian operator as given below.

$$\nabla_\perp^2 = \frac{1}{r}\frac{\partial}{\partial r}\left(r\frac{\partial}{\partial r}\right) + \frac{1}{r^2}\frac{\partial^2}{\phi^2} \tag{2.29}$$

By substituting the equation 2.28 into 2.24, we get:

$$\nabla_\perp^2 \vec{E}(x, y) + (k^2 - \beta^2)\vec{E}(x, y) = 0 \tag{2.30}$$

In which, the variation takes place only in the transverse directions. i.e. in the direction perpendicular to the direction of propagation. In the same way, we obtain for the magnetic field:

$$\nabla_\perp^2 \vec{H}(x, y) + (k^2 - \beta^2)\vec{H}(x, y) = 0 \tag{2.31}$$

The above given equations represent six second order differential equations with respect to each spatial component of electric $\vec{E}(x, y)$ and magnetic field $\vec{H}(x, y)$. The solutions of these component equations depends on transverse geometry and the boundary conditions at the interfaces of the dielectrics.

The electric field $\vec{E}(x, y)$ and magnetic field $\vec{H}(x, y)$ has three components each that make up to six components. All the components are not independent but are related. So in order to find these components, initially two components

can be taken as independent, using which the rest of the components can be found. The independent components considered are known as longitudinal components E_z and H_z. Once these components are known, using Maxwell's equations, the other 4 components such as E_x,E_y,H_x and H_y can be found.

To verify the relations between these components, we can make use of source free Maxwell's curl equations 2.13 and 2.14, upon expanding which, we get:

$$\frac{\partial E_z}{\partial y} + j\beta E_y = -j\omega\mu H_x \tag{2.32}$$

$$-j\beta E_x - \frac{\partial E_z}{\partial x} = -j\omega\mu H_y \tag{2.33}$$

$$\frac{\partial E_y}{\partial x} - \frac{\partial E_x}{\partial y} = -j\omega\mu H_z \tag{2.34}$$

$$\frac{\partial H_z}{\partial y} + j\beta H_y = -j\omega\epsilon E_x \tag{2.35}$$

$$-j\beta H_x - \frac{\partial H_z}{\partial x} = -j\omega\epsilon E_y \tag{2.36}$$

$$\frac{\partial H_y}{\partial x} - \frac{\partial H_x}{\partial y} = -j\omega\epsilon E_z \tag{2.37}$$

In the above equations, all the components are phasors that depend only on the variation in transverse directions. The partial derivatives with respect to z have been replaced by $-j\beta$. By manipulating these equations, we get four expressions for the transverse components.

$$E_x = -\frac{1}{k^2 - \beta^2}\left(j\beta\frac{\partial E_z}{\partial x} + j\omega\mu\frac{\partial H_z}{\partial y}\right) \tag{2.38}$$

$$E_y = -\frac{1}{k^2 - \beta^2}\left(j\beta\frac{\partial H_z}{\partial y} - j\omega\mu\frac{\partial H_z}{\partial x}\right) \tag{2.39}$$

$$H_x = -\frac{1}{k^2 - \beta^2}\left(j\beta\frac{\partial E_z}{\partial x} - j\omega\epsilon\frac{\partial E_z}{r\partial y}\right) \tag{2.40}$$

$$H_y = -\frac{1}{k^2 - \beta^2}\left(j\beta\frac{\partial H_z}{\partial y} + j\omega\epsilon\frac{\partial E_z}{\partial x}\right) \tag{2.41}$$

Once we find these components, we can use the equations 2.30 and 2.31 to analyze the wave behavior respectively. we can classify the waves propagating in a waveguide into three categories based on E_z and H_z.

1. If $E_z = 0$ and $H_z \neq 0$, then the modal field distribution is transverse in nature.

So these type of modes are called as TE or Transverse Electric modes.

2. If $E_z \neq 0$ and $H_z = 0$, then the modal field distribution does not contain the magnetic component. So these type of modes are called as TM or Transverse Magnetic modes.

3. If $E_z \neq 0$ and $H_z \neq 0$, then the modal field distributions are called as Hybrid modes.

Using these mode definitions, we proceed further to describe the concept of couple mode theory in next section.

2.2.2 Principle of Operation

According to [72], couplers are built on the understanding that the modal field extends beyond core and cladding region, so when the cores of two different fibers are brought sufficiently closer, the power inside the coupler shifts from one fiber to another, periodically. If the two fibers used in fabricating the coupler have same propagation constant, then the complete exchange of power takes place but if the fibers have different propagation constants, still the power shifts periodically but incompletely. We make use of coupled mode theory based on perturbation analysis as described in [73] to analyze the mode coupling between a regular and hollow core wave guides. Normally uniform waveguides contain numerous modes propagating through them. Due to multimode nature of SCF and HCF, several modes propagate in these waveguides. As part of simplification process, we considered lowest order modes shown in Fig. 2.3a and Fig. 2.3b from SCF and HCF to elaborate the power coupling process between these waveguides. We used COMSOL multiphysics software to simulate the modes in SCF and HCF and the modeling process is described in detail in chapter 3.

The individual modes propagating in SCF and HCF before getting coupled satisfy the Maxwell's curl equations 2.13 and 2.14

Let us assume that the propagating modes in SCF and HCF remain in same shape during the coupling process, though in reality there may be a slight deformation of modes when fibers are close to each other but still they get coupled.

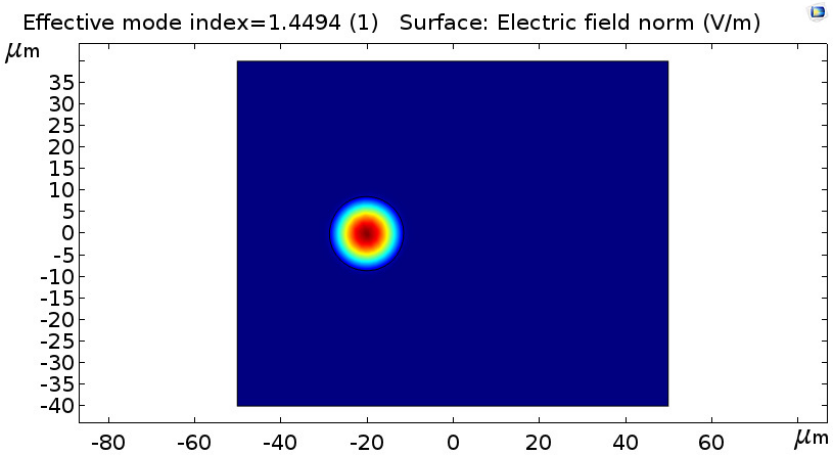

(a) One of the lowest order mode in SCF.

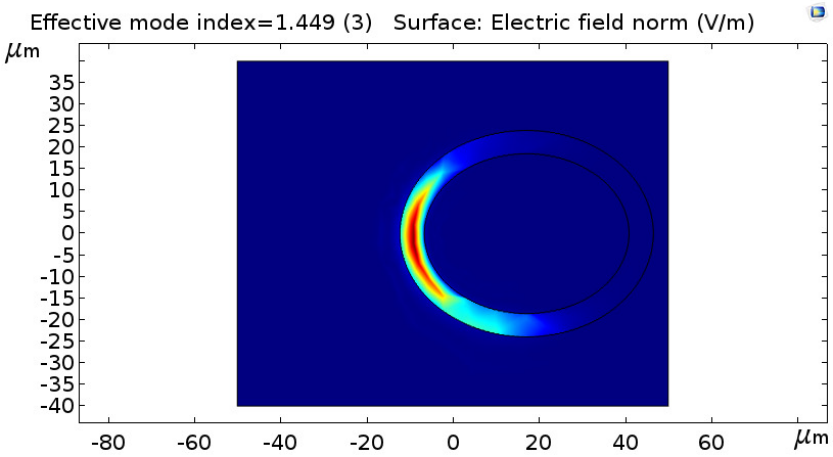

(b) One of the lowest order mode in HCF.

Figure 2.3: Modes in individual components of SCF-HCF coupler sensor.

Using this assumption, we can express total electric and magnetic field of our coupler as:

$$\vec{E}(x,y,z) = A(z)\vec{E}_{SCF}(x,y)e^{-j\beta_{SCF}z} + B(z)\vec{E}_{HCF}(x,y)e^{-j\beta_{HCF}z} \tag{2.42}$$

$$\vec{H}(x,y,z) = A(z)\vec{H}_{SCF}(x,y)e^{-j\beta_{SCF}z} + B(z)\vec{H}_{HCF}(x,y)e^{-j\beta_{HCF}z} \tag{2.43}$$

where $A(z)$, $B(z)$ are the amplitudes terms, which are functions of z. $\vec{E}_{SCF}(x,y,z)$, $\vec{E}_{HCF}(x,y,z)$, $\vec{H}_{SCF}(x,y,z)$ and $\vec{H}_{HCF}(x,y,z)$ are the field distributions in SCF and

HCF, which can be represented as:

$$\vec{E}_{SCF}(x,y,z) = \vec{E}_{SCF}(x,y)e^{-j\beta_{SCF}z} \tag{2.44}$$

$$\vec{E}_{HCF}(x,y,z) = \vec{E}_{HCF}(x,y)e^{-j\beta_{HCF}z} \tag{2.45}$$

$$\vec{H}_{SCF}(x,y,z) = \vec{H}_{SCF}(x,y)e^{-j\beta_{SCF}z} \tag{2.46}$$

$$\vec{H}_{HCF}(x,y,z) = \vec{H}_{HCF}(x,y)e^{-j\beta_{HCF}z} \tag{2.47}$$

in which β_{SCF} and β_{HCF} are the propagation constants of the individual modes propagating in SCF and HCF. Due to fact that SCF and HCF are multimode fibers, we considered a single mode among many other modes propagating through SCF and HCF.

In following sections, for convenience purposes we refer $\vec{E}_{SCF}$ as $\vec{E}_{SCF}(x,y)e^{-j\beta z}$ unless otherwise specified. We also adopt similar simplification to refer $\vec{H}_{SCF}$ as $\vec{H}_{SCF}(x,y)e^{-j\beta z}$, $\vec{E}_{HCF}$ as $\vec{E}_{HCF}(x,y)e^{-j\beta z}$ and $\vec{H}_{HCF}$ as $\vec{H}_{HCF}(x,y)e^{-j\beta z}$.

These individual modes get coupled when the wave guides are placed in close proximity. When power is supplied to SCF, the power is exchanged between modes of SCF and HCF as a function of z.

We substitute equations 2.42, 2.43 into 2.13, 2.14 to get

$$\nabla \times (A(z)\vec{E}_{SCF} + B(z)\vec{E}_{HCF}) = -j\omega\mu_0\vec{H} \tag{2.48}$$

$$\nabla \times (A(z)\vec{H}_{SCF} + B(z)\vec{H}_{HCF}) = j\omega\epsilon_0 n\vec{E} \tag{2.49}$$

After performing vector operations on 2.48 and 2.49 , we get (derivation steps included in Appendix A)

$$\frac{dA}{dz}(\hat{z} \times \vec{E}_{SCF}) + \frac{dB}{dz}(\hat{z} \times \vec{E}_{HCF}) = 0 \tag{2.50}$$

$$\frac{dA}{dz}(u_z \times \vec{H}_{SCF}) - j\omega\epsilon_0(n - n_{SCF})A\vec{E}_{SCF} + \frac{dB}{dz}(u_z \times \vec{H}_{HCF}) - j\omega\epsilon_0(n - n_{HCF})B\vec{E}_{HCF} = 0 \tag{2.51}$$

The left-hand side (LHS) of the equations 2.50 and 2.51 are substituted in below

given general integral equations[73].

$$\int_{-\infty}^{\infty}\int_{-\infty}^{\infty}[\vec{E}^*_{SCF}\cdot(LHS\,of\,eq.\,2.51)-\vec{H}^*_{SCF}\cdot(LHS\,of\,eq.\,2.50)]dxdy=0 \quad (2.52)$$

$$\int_{-\infty}^{\infty}\int_{-\infty}^{\infty}[\vec{E}^*_{HCF}\cdot(LHS\,of\,eq.\,2.51)-\vec{H}^*_{HCF}\cdot(LHS\,of\,eq.\,2.50)]dxdy=0 \quad (2.53)$$

The steps involving expanding and arranging these equations are given in the appendix. The resultant equations are:

$$\begin{aligned}&\frac{dA}{dz}+\frac{dB}{dz}\frac{\int_{-\infty}^{\infty}\int_{-\infty}^{\infty}\hat{z}\cdot[(\vec{E}^*_{SCF}\times\vec{H}_{HCF})+(\vec{E}_{HCF}\times\vec{H}^*_{SCF})]dxdy}{\int_{-\infty}^{\infty}\int_{-\infty}^{\infty}\hat{z}\cdot[(\vec{E}^*_{SCF}\times\vec{H}_{SCF})+(\vec{E}_{SCF}\times\vec{H}^*_{SCF})]dxdy}\\&+jA\frac{\omega\epsilon_0\int_{-\infty}^{\infty}\int_{-\infty}^{\infty}(n-n_{SCF})\vec{E}_{SCF}\cdot\vec{E}^*_{SCF}dxdy}{\int_{-\infty}^{\infty}\int_{-\infty}^{\infty}\hat{z}\cdot[(\vec{E}^*_{SCF}\times\vec{H}_{SCF})+(\vec{E}_{SCF}\times\vec{H}^*_{SCF})]dxdy}\\&+jB\frac{\omega\epsilon_0\int_{-\infty}^{\infty}\int_{-\infty}^{\infty}(n-n_{HCF})B\vec{E}_{HCF}\cdot\vec{E}^*_{SCF}dxdy}{\int_{-\infty}^{\infty}\int_{-\infty}^{\infty}\hat{z}\cdot[(\vec{E}^*_{SCF}\times\vec{H}_{SCF})+(\vec{E}_{SCF}\times\vec{H}^*_{SCF})]dxdy}=0\end{aligned} \quad (2.54)$$

$$\begin{aligned}&\frac{dB}{dz}+\frac{dA}{dz}\frac{\int_{-\infty}^{\infty}\int_{-\infty}^{\infty}\hat{z}\cdot[(\vec{E}^*_{HCF}\times\vec{H}_{SCF})+(\vec{E}_{SCF}\times\vec{H}^*_{HCF})]dxdy}{\int_{-\infty}^{\infty}\int_{-\infty}^{\infty}\hat{z}\cdot[(\vec{E}^*_{HCF}\times\vec{H}_{HCF})+(\vec{E}_{HCF}\times\vec{H}^*_{HCF})]dxdy}\\&+jA\frac{\omega\epsilon_0\int_{-\infty}^{\infty}\int_{-\infty}^{\infty}(n-n_{SCF})\vec{E}_{SCF}\cdot\vec{E}^*_{SCF}dxdy}{\int_{-\infty}^{\infty}\int_{-\infty}^{\infty}\hat{z}\cdot[(\vec{E}^*_{HCF}\times\vec{H}_{HCF})+(\vec{E}_{HCF}\times\vec{H}^*_{HCF})]dxdy}\\&+jB\frac{\omega\epsilon_0\int_{-\infty}^{\infty}\int_{-\infty}^{\infty}(n-n_{HCF})\vec{E}_{HCF}\cdot\vec{E}^*_{SCF}dxdy}{\int_{-\infty}^{\infty}\int_{-\infty}^{\infty}\hat{z}\cdot[(\vec{E}^*_{HCF}\times\vec{H}_{HCF})+(\vec{E}_{HCF}\times\vec{H}^*_{HCF})]dxdy}=0\end{aligned} \quad (2.55)$$

As per [73], to separate transverse and axial dependencies of electromagnetic fields, we make use of equations 2.44 - 2.47 and substitute them in the above equations to

get:

$$\frac{dA}{dz}+\frac{dB}{dz}\frac{\int_{-\infty}^{\infty}\int_{-\infty}^{\infty}\hat{z}\cdot[(E^*_{SCF}(x,y)\times H_{HCF}(x,y))+(E_{HCF}(x,y)\times H^*_{SCF}(x,y))]dxdy}{\int_{-\infty}^{\infty}\int_{-\infty}^{\infty}\hat{z}\cdot[(E^*_{SCF}(x,y)\times H_{SCF}(x,y))+(E_{SCF}(x,y)\times H^*_{SCF}(x,y))]dxdy}$$
$$\cdot e^{[-j(\beta_{HCF}-\beta_{SCF})z]}$$
$$+jA\frac{\omega\epsilon_0\int_{-\infty}^{\infty}\int_{-\infty}^{\infty}(n-n_{SCF})E_{SCF}(x,y)\cdot E^*_{SCF}(x,y)dxdy}{\int_{-\infty}^{\infty}\int_{-\infty}^{\infty}\hat{z}\cdot[(E^*_{SCF}(x,y)\times H_{SCF}(x,y))+(E_{SCF}(x,y)\times H^*_{SCF}(x,y))]dxdy}$$
$$+jB\frac{\omega\epsilon_0\int_{-\infty}^{\infty}\int_{-\infty}^{\infty}(n-n_{HCF})E_{HCF}(x,y)\cdot E^*_{SCF}(x,y)dxdy}{\int_{-\infty}^{\infty}\int_{-\infty}^{\infty}\hat{z}\cdot[(E^*_{SCF}(x,y)\times H_{SCF}(x,y))+(E_{SCF}(x,y)\times H^*_{SCF}(x,y))]dxdy}$$
$$\cdot e^{[-j(\beta_{HCF}-\beta_{SCF})z]}=0 \tag{2.56}$$

$$\frac{dB}{dz}+\frac{dA}{dz}\frac{\int_{-\infty}^{\infty}\int_{-\infty}^{\infty}\hat{z}\cdot[(E^*_{HCF}(x,y)\times H_{SCF}(x,y))+(E_{SCF}(x,y)\times H^*_{HCF}(x,y))]dxdy}{\int_{-\infty}^{\infty}\int_{-\infty}^{\infty}\hat{z}\cdot[(E^*_{HCF}(x,y)\times H_{HCF}(x,y))+(E_{HCF}(x,y)\times H^*_{HCF}(x,y))]dxdy}$$
$$\cdot e^{[j(\beta_{HCF}-\beta_{SCF})z]}$$
$$+jA\frac{\omega\epsilon_0\int_{-\infty}^{\infty}\int_{-\infty}^{\infty}(n-n_{SCF})E_{SCF}(x,y)\cdot E^*_{SCF}(x,y)dxdy}{\int_{-\infty}^{\infty}\int_{-\infty}^{\infty}\hat{z}\cdot[(E^*_{HCF}(x,y)\times H_{HCF}(x,y))+(E_{HCF}(x,y)\times H^*_{HCF}(x,y))]dxdy}$$
$$\cdot e^{[j(\beta_{HCF}-\beta_{SCF})z]}$$
$$+jB\frac{\omega\epsilon_0\int_{-\infty}^{\infty}\int_{-\infty}^{\infty}(n-n_{HCF})E_{HCF}(x,y)\cdot E^*_{SCF}(x,y)dxdy}{\int_{-\infty}^{\infty}\int_{-\infty}^{\infty}\hat{z}\cdot[(E^*_{HCF}(x,y)\times H_{HCF}(x,y))+(E_{HCF}(x,y)\times H^*_{HCF}(x,y))]dxdy}=0 \tag{2.57}$$

which can be simplified into

$$\frac{dA}{dz}+c_{12}\frac{dB}{dz}e^{[-j(\beta_2-\beta_1)z]}+jA\chi_1+jB\kappa_{12}e^{[-j(\beta_2-\beta_1)z]}=0 \tag{2.58}$$
$$\frac{dB}{dz}+c_{21}\frac{dA}{dz}e^{[j(\beta_2-\beta_1)z]}+jB\chi_2+jA\kappa_{21}e^{[j(\beta_2-\beta_1)z]}=0 \tag{2.59}$$

where 1 is SCF, 2 is HCF and c_{12}, χ_1, κ_{12} are given as:

$$c_{12} = \frac{\int_{-\infty}^{\infty}\int_{-\infty}^{\infty} \hat{z} \cdot [(E^*_{SCF}(x,y) \times H_{HCF}(x,y)) + (E_{HCF}(x,y) \times H^*_{SCF}(x,y))]dxdy}{\int_{-\infty}^{\infty}\int_{-\infty}^{\infty} \hat{z} \cdot [(E^*_{SCF}(x,y) \times H_{SCF}(x,y)) + (E_{SCF}(x,y) \times H^*_{SCF}(x,y))]dxdy} \tag{2.60}$$

$$\chi_1 = \frac{\omega\epsilon_0 \int_{-\infty}^{\infty}\int_{-\infty}^{\infty}(n - n_{SCF})E_{SCF}(x,y) \cdot E^*_{SCF}(x,y)dxdy}{\int_{-\infty}^{\infty}\int_{-\infty}^{\infty} \hat{z} \cdot [(E^*_{SCF}(x,y) \times H_{SCF}(x,y)) + (E_{SCF}(x,y) \times H^*_{SCF}(x,y))]dxdy} \tag{2.61}$$

$$\kappa_{12} = \frac{\omega\epsilon_0 \int_{-\infty}^{\infty}\int_{-\infty}^{\infty}(n - n_{HCF})E_{HCF}(x,y) \cdot E^*_{SCF}(x,y)dxdy}{\int_{-\infty}^{\infty}\int_{-\infty}^{\infty} \hat{z} \cdot [(E^*_{SCF}(x,y) \times H_{SCF}(x,y)) + (E_{SCF}(x,y) \times H^*_{SCF}(x,y))]dxdy} \tag{2.62}$$

Equations 2.58 and 2.59 represent the generalized coupled mode equations and they are used to describe the coupling between SCF and HCF wave guides. c_{12}, χ_1 and κ_{12} are called as butt coupling coefficient, change in propagation constant and mode coupling coefficient.

The mode coupling coefficient actually describes how quickly the power exchange takes place between SCF and HCF. It can also be considered as the parameter that explains how efficiently the power leaks or couples from SCF to HCF. The butt coupling coefficient c_{12} is described in [73] as the electromagnetic field excitation efficiency at point $z = 0$ from SCF placed in the region $z < 0$ to HCF placed in the region $z \geq 0$. The last term is χ_1, which is change in propagation constant and it describes how much the propagation constant of a mode in SCF is affected or changed by the mode overlapping from the higher order mode propagating in HCF. Assuming the change in propagation constant is very less, we consider $\chi_1 = 0$.

As per [73], c_{12} and χ_1 are considered as zero values when mode coupling effect is not considered strictly.

As per [54], at resonance the coupling coefficients κ_{12} and κ_{21} are related through,

$$\kappa = \kappa_{12} = \kappa^*_{21} = \frac{\omega\epsilon_0}{4P_0}\int\int(n - n_{HCF})E^*_{SCF}(x,y) \cdot E_{HCF}(x,y)dxdy \tag{2.63}$$

in which, ω is the angular wave frequency, P_0 unit power carried by normalized fields,

ϵ_0 is the permittivity of free space, n is the RI distribution of SCF-HCF coupler, n_{HCF} is the RI distribution of HCF, $E^*_{SCF}(x,y)$ and $E_{HCF}(x,y)$ are the normalized field distributions.

The power flowing through SCF or HCF modes can be calculated using below expression as per [73].

$$P_p = \frac{1}{2}\int_{-\infty}^{\infty}\int_{-\infty}^{\infty}(E_p \times H_p^*)\cdot u_z dxdy \tag{2.64}$$

In which, p is SCF or HCF. The power flowing through these wave guides is normalized to carry $1W$, such that when power is periodically exchanging between SCF and HCF, the probability of power flowing through SCF or HCF can be estimated in the range of $0(0\%)$ to $1W(100\%)$. As per [74], a function $\psi(r,t)$ is said to be normalized when square of that function when integrated over a set of coordinates within the total volume V, gives us a value of 1. The mathematical probability distribution is given as $\int_V(|\psi(r,t)|^2)dV = 1$. Generally, normalizing a wave function means multiplying it by a constant to make sure that the sum of its probabilities for finding the particle equals to 1.

We make use of a constant α and by multiplying it with power flowing through SCF or HCF, the power can be normalized to $1W$.

The normalized power is used as unit power P_0 flowing in the wave guides given in equation 2.63.

$$(\alpha^2)P_p = 1 \tag{2.65}$$

$$\alpha = \frac{1}{\sqrt{P_p}} \tag{2.66}$$

When light with power P_{in}^{SCF} is delivered to the input end of SCF, it will be gradually transferred to the HCF.

$$\frac{P_{out}^{SCF}}{P_{in}^{SCF}} = 1 - \frac{\kappa^2}{q^2}\sin^2(qz) \tag{2.67}$$

where P_{in}^{SCF} is the power launched in SCF at $z = 0$, P_{out}^{SCF} and $P^{HCF}(z)$ are the powers propagating in SCF and HCF and q is:

$$q = \sqrt{\kappa^2 + \delta^2} \tag{2.68}$$

δ is the propagation constants mismatch between the modes of SCF and HCF with propagation constants β_1 and β_2 of the optical fibers in the coupler and it is given as

$$\delta = (\beta_2 - \beta_1)/2 \tag{2.69}$$

The max power coupling efficiency is given as η_{max}

$$\eta_{\max} = (\frac{\kappa^2}{q^2}) \tag{2.70}$$

The light power, after interacting with the test samples in the hollow core of HCF, will be transferred back to the SCF after reaching its maximum at $z = \frac{\pi}{2q}$ in HCF. Assuming the coupler has a effective coupling length L_c, the portion of light power exit the SCF output port will be $\frac{\kappa^2}{\gamma^2}\sin^2(qz)$ here. Noting that the output power is a determined κ and δ, when liquid with slightly different refractive index flowing through the HCF core, the output power will be dominant by δ, which approximately proportional to the liquid refractive index. Therefore, by monitoring the output power change one may determine the refractive index of the liquid injected to the HCF.

Chapter 3

Modeling of SCF-HCF coupler

3.1 Modeling in comsol

Modeling is defined as an art of numerically solving a physical system and it's phenomena. It can also be referred as a graphical simulation. Comsol multi-physics is one powerful interactive modeling toolkit and it uses finite element analysis (FEA) method to solve many scientific and engineering problems. There are several modules available in comsol multi-physics for various types of analyses. Optics is one such module used for electromagnetic modeling of wave guides and optical fibers. Under optics there are two sub modules and they are ray optics and wave optics. We chose wave optics as they offer interfaces that are apt for electromagnetic modeling of optical wave guides. One such interface is electromagnetic waves, frequency domain and it supports various study types such as frequency domain, mode analysis, eigen frequency, boundary mode analysis and frequency domain. Mode analysis study type is used to compute propagation constants and propagating mode shapes, so it is used for numerically solving the SCF-HCF coupler.

As per the theory stated in previous chapter, the exchange of power between SCF and HCF is analyzed and will be simulated as part of the modeling. Firstly a project has to be created for study of modal analysis. Further steps for modeling are outlined as follows:

1. Creating a model with appropriate geometry: The coupler geometry has a cross section view and it is drawn using geometric objects such as rectangle, circle etc.

2. Choosing right physics: It defines model equations, boundary conditions, materials properties and initial conditions.

3. Meshing: The model is subdivided into size specific triangular elements. Meshing can be either a physics controlled or user defined and it depends upon the modeling requirement.

4. Selecting the type of study: The study is used to analyze and solve the model.

5. Post processing and analysis: The analysis includes calculation of parameters such as the propagation constant, coupling co-efficient etc. and plotting modal fields respetively.

Comsol multi-physics is capable of solving 2D and 3D models. In this chapter, an approach towards 2D modeling of a SCF-HCF directional coupler with detailed explanation has been covered. In order to verify the results obtained by simulating SCF-HCF coupler, a SCF-SCF directional coupler was modeled and the results were taken as a reference to validate the SCF-HCF results qualitatively.

3.2 SCF-SCF directional coupler model

The SCF-SCF directional coupler is modeled as two independent components, each component representing a wave guide with modes. After building model geometry of both the components, they are solved to obtain the modes and eventually they are coupled by placing the wave guides in a close proximity.

3.2.1 Geometry and materials

The 2D model of SCF-SCF directional coupler is a cross section view of the coupler and it was modeled as two separate components. Some parameters are defined in

parameters section under global definitions to access them in required sub sections of the model tree. Table 3.1 shows the parameters used for drawing the model geometry. Each component of SCF-SCF directional coupler model has a solid fiber

Table 3.1: Required parameters for drawing SCF-SCF directional coupler model geometry.

Parameter	**Value**
Refractive index of SCF core	1.456
Refractive index of SCF cladding	1.450
SCF core radius	$4.1\,\mu m$
SCF cladding length	$30\,\mu m$
SCF cladding height	$20\,\mu m$
Separation between SCF cores	$10\,\mu m$

core embedded in a rectangular cladding material. The cladding material has a side length of $30\,\mu m$ and height of $20\,\mu m$. The embedded core has a radius of $4.1\,\mu m$. Upon overlapping the two components, cores in both the components are separated by $10\,\mu m$.

Once the geometry of the directional coupler model is drawn, components of the model are assigned with appropriate materials. The cores and cladding are made up of same material, which is silica glass and it is available under built-in materials under materials section. However, the refractive index of core and cladding is different. The core refractive index is higher than that of the cladding and the values of refractive indices of core and cladding are defined in the parameters section.

3.2.2 Meshing and study

Meshing in FEA refers to dividing the model geometry into small pieces or elements that are connected by nodes. All the elements are solved individually that leads to creating a complete solution. A mesh can be created in two ways such as physics controlled and user defined. Physics controlled mesh is used for adding mesh to SCF-SCF directional coupler model and its settings are defined under physics of the model. In the settings of physics controlled mesh, the mesh element size control is an user defined parameter and a value of $2\,\mu m$ is defined. The value defined produces a finer mesh and does not affect the processing time and produces an accurate solution. After

Table 3.2: Required parameters and values for computing mode analysis study.

Parameter	Value
Speed of light (c)	$2.9979 \times 10^8 m/s$
Wavelength of light (λ)	$0.98 \mu m$
Mode analysis frequency ($\frac{c}{\lambda}$)	$3.0591 \times 10^{14} Hz$
Desired number of modes	4
Search for modes around refractive index	1.456

configuring settings, mesh is created by clicking build all under mesh section of the model. The mesh is applied on first component model and same steps are repeated for the other component model. After applying mesh on both the component models, they look as shown in Fig. 3.1. Computation time increases as the number of smaller elements of the model increase. So as to reduce the computation time, mesh is created with fewer number of elements by choosing $2\,\mu m$ as the element size and as a result the time took to compute the study is 7 seconds. The study used to find the modes in the individual components is called mode analysis. The parameter values for computing mode analysis are given in table 3.2. This step is performed for both the coupler components and eventually these modes are coupled.

3.2.3 Results and post-processing

After completing the mode analysis, a total of 6 modes are generated in each individual component. To calculate the coupling co-efficient and exchange of power between the wave guides, the fundamental mode of both the wave guides in close proximity are taken into consideration. The electric field norm of the fundamental mode of both the wave guides are shown in the Fig. 3.2.

Coupling coefficient

When two wave guides are in close proximity and if one of the wave guide is excited with light energy, it propagates in z direction and slowly starts leaking into the adjacent wave guide and at one point, the complete light would leak into the second wave guide and keeps propagating. After some point in z dimension of the second wave guide, light starts leaking back into the first wave guide and this process repeats.

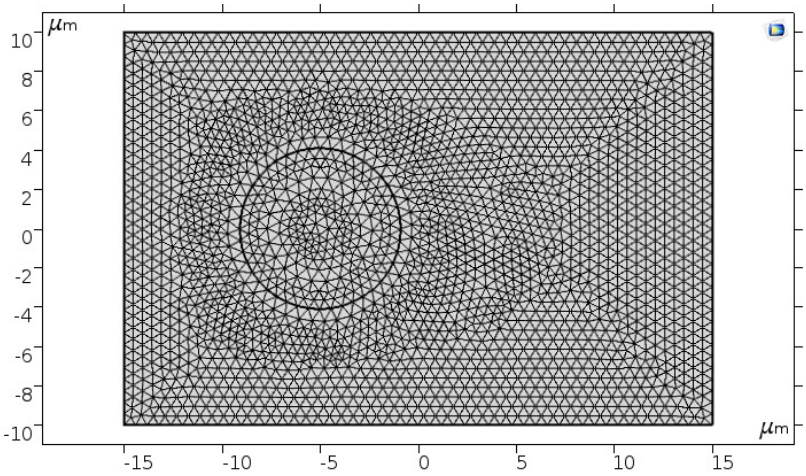

(a) Meshing applied to left fiber 2D model of SCF-SCF directional coupler.

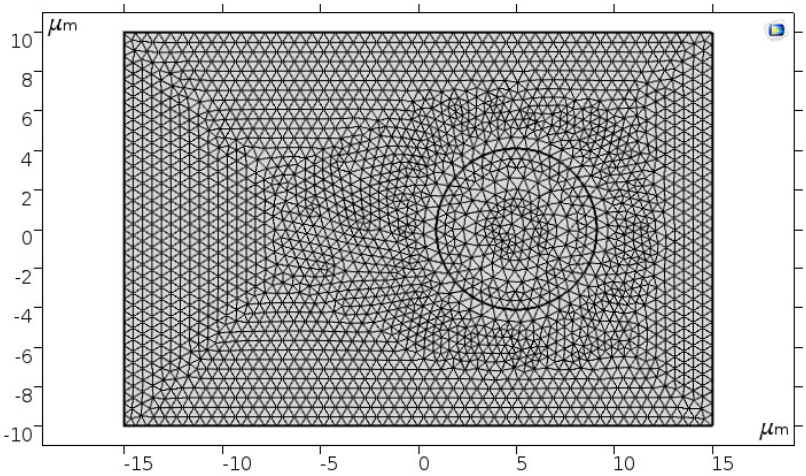

(b) Meshing applied to right fiber 2D model of SCF-SCF directional coupler.

Figure 3.1: Meshing applied to individual components of SCF-SCF directional coupler 2D model.

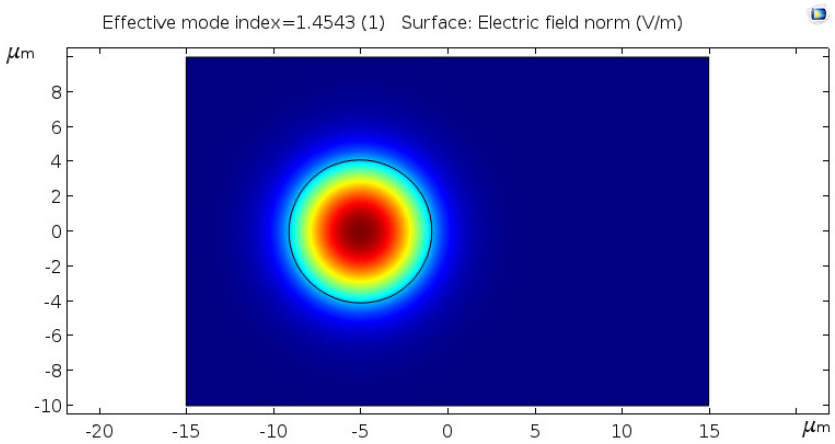

(a) Electric field norm obtained from left fiber 2D model of SCF-SCF directional coupler.

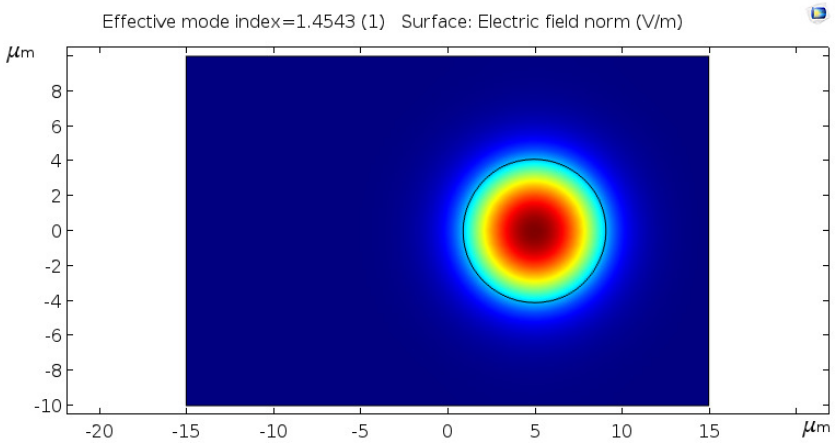

(b) Electric field norm obtained from right fiber 2D model of SCF-SCF directional coupler.

Figure 3.2: Electric field norm from individual components of SCF-SCF directional coupler 2D model.

Thus a periodic exchange of power takes place between the wave guides as a function of z.

The mode coupling coefficient given in equation 2.63 states how efficiently power can leak into the adjacent wave guide from the source wave guide and it is was derived in the previous chapter. The field distributions in both the wave guides are normalized to carry unit power. Initially the power flowing through the wave guide is calculated using the equation 2.64. The obtained power of the wave guide is then normalized to $1W$ using a co-efficient α from equation 2.66. The data sets obtained from both the components are joined using a join operator under data sets section of results. The data sets of both the components are joined with explicit method, so that a particular data set can be accessed using data1() and data2(). Using the joined data set, the normalized fields of both the wave guides and other parameters in the expression are used in calculating the mode coupling co-efficient. The surface integration operator available under derived values is used to solve the expression. The coupling co-efficient value obtained is $1129.027\,m^{-1}$.

Using data1() and data2(), the propagation constants of both the fibers are used to find difference in the propagation constant, which is δ as per [73]. The global evaluation section is used to calculate δ and the value obtained is $6.94 \times 10^{-4}\,m^{-1}$, which is very less and it can considered as a zero, i.e. $\delta = 0$.

$$\delta = \frac{(\beta_2 - \beta_1)}{2} \tag{3.1}$$

As per [73], when the propagation constants of both the fibers are equal, power from first wave guide couples 100% into the second wave guide and the length at which the complete transfer of power takes place is called as coupling length (L_c) and it is expressed as,

$$L_c = \frac{\pi}{2\kappa} \tag{3.2}$$

Using coupling coefficient κ, the minimum coupling length is calculated and the value obtained is $1.4\,mm$. After analyzing the minimum coupling length, the length of fiber in terms of z is assumed to be $3\,mm$ and a plot of power flow against the length of the wave guides is plotted as shown in Fig. 3.3.

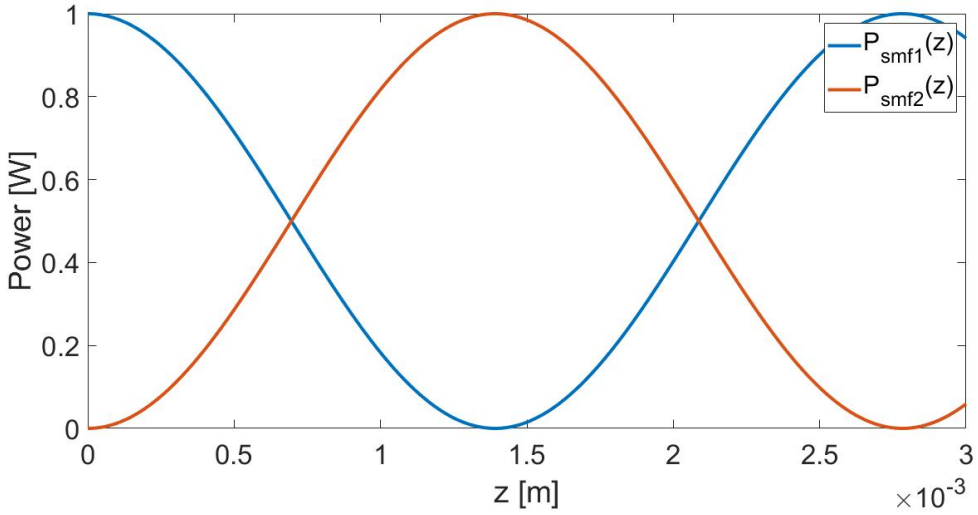

Figure 3.3: Exchange of power in SCF-SCF directional coupler.

Mode Matching - Different approach

When two SCF's are placed in close proximity, the modes propagating in the both the fibers interfere. In this scenario, the coupled waveguides act as one single wave guide with two different cores and thus this structure will have two modes propagating through them and they are symmetric and antisymmetric modes. Symmetric mode is the fundamental mode. However, these two modes will have different propagation constants such that when one wave guide is supplied with normalized power, the similar lobes of the modes sum up and the contrasting lobes cancel out as the modes propagate. Due to difference in the propagation constants of the modes, as they propagate they develop a phase difference. When the phase difference reaches π, the complete power will switch to second wave guide and as a result the first wave guide will have no power propagating through it. After a phase difference of 2π, the complete power switches back to first wave guide and this process repeats periodically and results in periodic exchange of power between the wave guides.

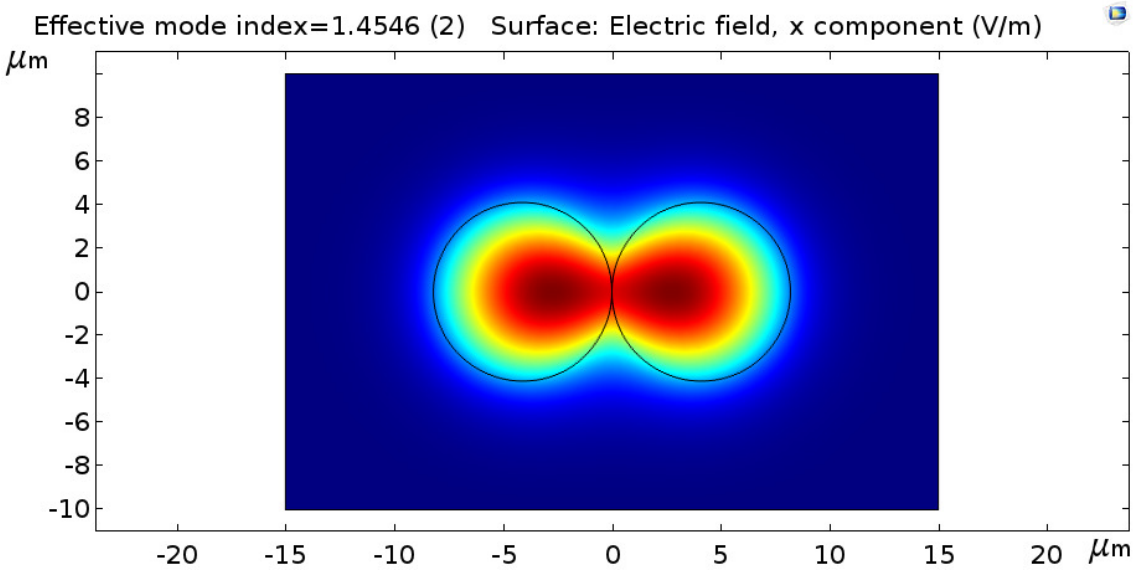

(a) Symmetric mode propagating through SCF-SCF coupler.

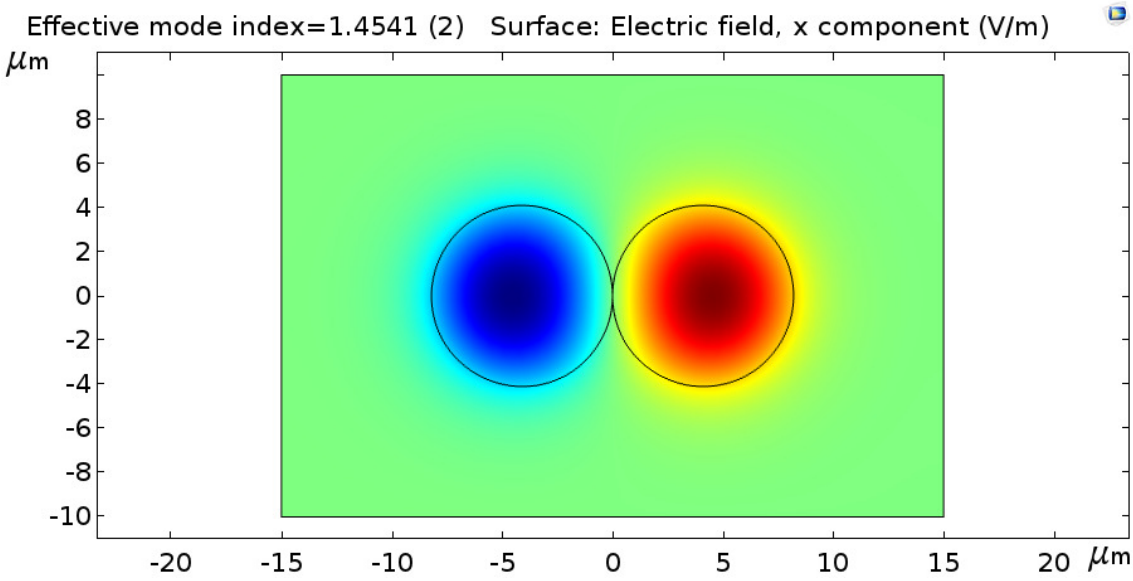

(b) Anti-Symmetric mode propagating through SCF-SCF coupler.

Figure 3.4: Two modes with different propagation constant propagating through SCF-SCF coupler 2D model.

3.3 SCF-HCF coupler

3.3.1 Scanning Electron Microscopy (SEM)

Scanning electron microscope (SEM) provides high spatial resolution and is very useful in capturing images of minute structures. SEM generates images through scanning the surface by electrons. These electrons hit the surface and generate various impulses, which are converted in to a meaningful graphical information.

The coupler shown in Fig. 3.4a was used to capture the images using SEM. Initially the coupler was fabricated using flame brush technique. The coupler is held tightly by the clamps of fiber pulling stage and a microscopic glass slide is inserted underneath the coupler along the axis and carefully moved closer to the coupler until it just touches the glass slide. Epoxy was used to glue the opposite ends of the fiber coupler to the glass slide. Using a optical fiber cleaver, a scratch was made on the coupler junction to cut it into two halves. Next, the glass slide underneath the coupler junction was broken to separate two halves. One of the half was used as a sample to capture the images which can clearly display the edges of SCF and HCF at high resolution.

In order to make the sample more conductive, it was coated with Ion Beam sputterer. Later the coated sample was placed on a 45^0 angled SEM stage, such that the stage can freely rotate and place the sample tip vertical to the electron beam. The sample was held tight by knobs of the SEM stage.

Using the appropriate settings of working distance, voltage and current values, images were taken as shown in the Fig. 3.4. The beam current was lowered significantly to reach high resolution. Initially using a high mag mode setting of SEM, the sample tip was identified and then using low mag mode, the view was zoomed in. The beam was aligned and focused on the sample to take the best possible images. Further the magnification was increased to take high resolution images. The steps were repeated to take multiple images in different angles.

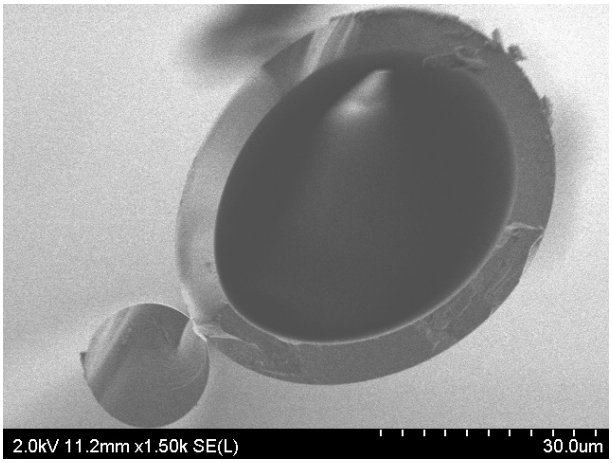

(a) Cross section of SCF-HCF coupler.

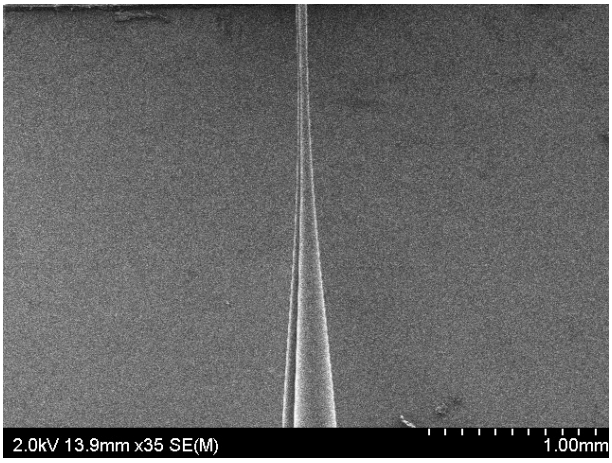

(b) Longitudinal section of SCF-HCF coupler.

Figure 3.5: SEM images of SCF-HCF coupler.

3.4 SCF-HCF coupler sensor model

The SCF-HCF coupler sensor was modeled in the same way as SCF-SCF directional coupler but the only change made in SCF-HCF coupler was to replace the second solid core fiber with an elliptical hollow core fiber. The measurements used in drawing shapes of SCF and HCF are taken from scanning electron microscope (SEM) images of SCF-HCF coupler cross section. The modeled structure consists of two components and each component has a rectangular block, which acts as PDMS (Polydimethylsiloxane), forming the cladding of both the wave guides. The first component has a rectangular PDMS material housing SCF, which has only cladding material of diameter $17.2\,\mu m$. The second component consists of a rectangular PDMS and a embedded HCF with a wall thickness of $5\,\mu m$. Since SCF core diameter is very small and due to reason of higher concentration of mode in cladding of SCF, core of SCF is not considered in the model. The parameters used for drawing model geometry are saved in the parameters section under global definitions are shown in table 3.3. The structured

Table 3.3: Required parameters and values for building SCF-HCF directional coupler model geometry.

Parameter	**Value**
Refractive index of SCF core	1.45
Refractive index of HCF core	1.451
Refractive index of PDMS	1.41
SCF core radius	$8.6\mu m$
PDMS height	$100\,\mu m$
PDMS	$80\,\mu m$
separation	$37.15\,\mu m$

model is added with appropriate materials. The rectangular block acts as a PDMS and its refractive index at a wavelength of $0.98\,\mu m$ is 1.41 and to fibers are assigned with silica glass. However, the refractive index of silica glass of SCF is 1.45, whereas the refractive index of silica glass of HCF wall is 1.451. Physics controlled mesh with user defined value of $2\mu m$ is applied to both the SCF-HCF coupler components and the final meshed model shown in Fig. 3.5. The computation time to solve the model took a minimal time of $2 seconds$. The required parameters and the values for solving both the components for modes are given in table 3.4 and table 3.5. After computing mode analysis on both the components, electric field norm obtained and

Table 3.4: Required parameters and values for computing mode analysis on SCF of SCF-HCF coupler sensor.

Parameter	**Value**
Speed of light (c)	$2.9979 \times 10^8 m/s$
Wavelength of light (λ)	$0.98 \mu m$
Mode analysis frequency ($\frac{c}{\lambda}$)	$3.0591 \times 10^{14} Hz$
Desired number of modes	6
Search for modes around refractive index	1.45

Table 3.5: Required parameters and values for computing mode analysis on HCF of SCF-HCF coupler sensor.

Parameter	**Value**
Speed of light (c)	$2.9979 \times 10^8 m/s$
Wavelength of light (λ)	$0.98 \mu m$
Mode analysis frequency ($\frac{c}{\lambda}$)	$3.0591 \times 10^{14} Hz$
Desired number of modes	6
Search for modes around refractive index	1.451

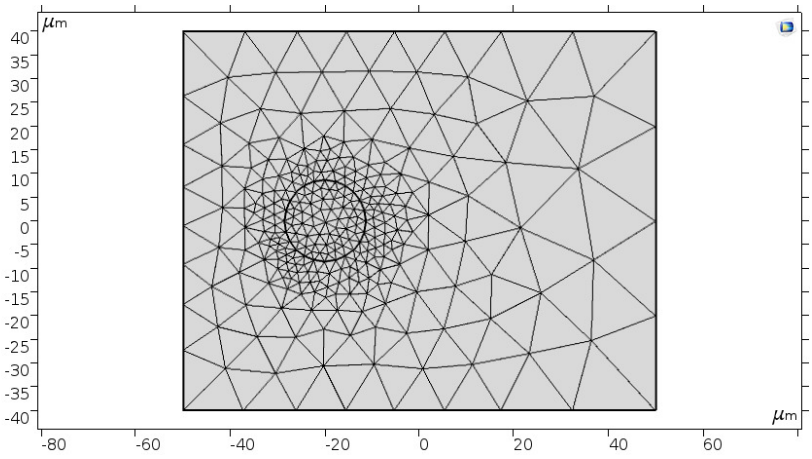

(a) Mesh applied to SCF of SCF-HCF coupler sensor.

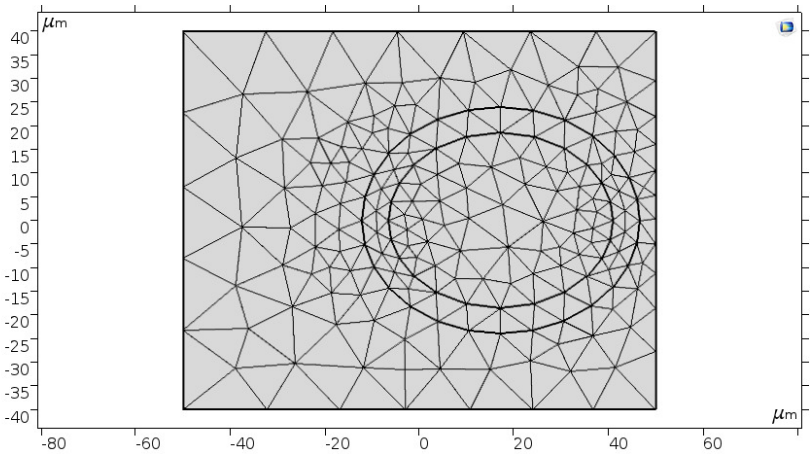

(b) Mesh applied to HCF of SCF-HCF coupler sensor.

Figure 3.6: Meshing applied to Individual components of SCF-HCF coupler sensor model.

is shown in Fig. 2.3. Using the procedure described in previous section, coupling coefficient (κ) and difference in propagation constant (δ) for SCF-HCF coupler sensor were calculated and they are $1482.22\,m^{-1}$ and $-1252.18\,m^{-1}$ respectively. Since the difference in the propagation constant is significant, the power from SCF does not leak completely into HCF. Fig. 3.6 shows a plot of power flow in SCF and HCF as a function of z.

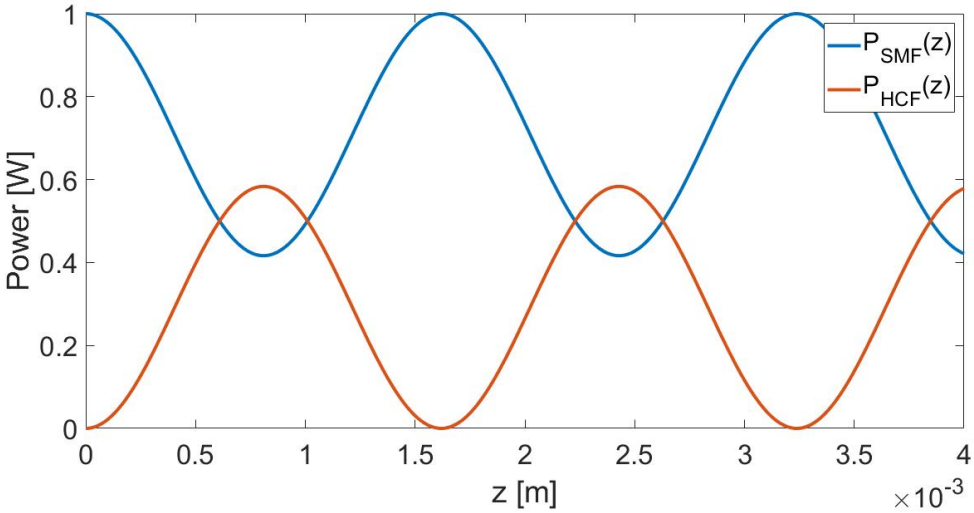

Figure 3.7: Exchange of power among adjacent SCF and HCF in a SCF-HCF coupler sensor.

Chapter 4

Fabrication of Sensor

4.1 Preparing fibers for fabrication

4.1.1 Polyimide coating removal methods

The silica capillary tubing comes with polyimide coating to protect the fiber from abrasion. Some sensing applications require this coating to be removed. There are wide number of methods available to remove this coating and some of them are thermal techniques, laser and mechanical processes.

Thermal techniques

- **Flame Sources**: Several flame sources such as matches, lighters, hydrogen, oxygen and propane can be used to remove the coating on the tube. This procedure has to be followed carefully as it can make fiber brittle and vulnerable to break.
- **Sulfuric Acid**: When sulfuric acid is heated up to $150°C$, it can remove polyimide coating of immersed HCF in 2 to 5 minutes. This method is mostly recommended for applications that require precise coating removal and residue free process.

- **Etching**: Sodium hydroxide and Hydrofluoric acid (HF) can remove the polyimide coating but also tend to etch the inner glass surface. This method is not recommended for the applications requiring fiber strength and stability.

Lasers

- **CO_2 Laser**: This type of laser burns polyimide coating. However, this method requires greater precision and control over the burning process.

Mechanical processes

- **Machining**: Several tools are used to strip off the polyimide coating. Some of the tools are X-Acto knife, razor blade or cutting tool. This method is highly not recommended for sensing applications as the friction caused while stripping off the coating can cause cracks on the tubing walls , making them vulnerable to break.

4.1.2 HCF Cleaving methods

Cleaving is a process which involves cutting the fiber precisely to separate the fiber into two halves. Cutting an optical fiber is a similar process as cutting a glass. The method involves making a scratch on a fiber and upon applying pressure, the scratched part breaks in a smooth manner. Before making a scratch, the cutting blade must be placed perpendicular to the fiber axis so as to avoid slant edges or protruding glass on the edges of the fiber.

Many applications require minimal lengths of the fiber and typically it may range up to few centimeters long. A well suited cleaving procedure must be followed to get smooth edges on the cut surface. As per [75], there are four cleaving procedures outlined and they are standard cleaving, precision cleaving, saw and laser cutting.

4.2 Methods of Fabricating Directional Couplers

Optical fibers are made up of glass and are made up of layers of glass with different doping concentrations. Optical fibers have a core region with highest refractive index and light propagates in this region. The core region is protected by cladding layer with refractive index less than that of the core. Further, the cladding is surrounding by a coating to protect the fiber from high abrasion and to provide flexibility. In a directional coupler, light from core region of fiber 1 has to reach the core region of fiber 2 for a successful coupling and in order to achieve this, the coating has to be removed and the cladding has to be made sufficiently thin, such that the light can leak out of the core and interact with the core of adjacent fiber. Couple of the methods to build a directional coupler are outlined in this chapter.

Flame Brush Method

The flame brush method involves a heating source, fiber puller stage and a display mechanism to view the output variations while fabricating a coupler.

Initially the protective coating is removed from both the fibers and are twisted together at their respective coating free regions and then they are mounted on a fiber pulling stage. The twisted fiber pair is held tight by the clamps as shown in the Fig. 4.1. It is very important to clean and align the fibers on the fiber pulling stage to obtain an efficient and low loss coupler. Once fibers are stabilized on the pulling stage, hydrogen flame is turned on and maintained at a specific flow rate. If the flame with a particular flow rate is constant, the fiber pulling stage is activated. The two opposite clamps of the stage move away in the opposite directions, thus stretching the twisted pair of fibers to create a thin junction in the center. During this process, a periodic drop and rise of the power takes place inside the fibers, which can be verified from an oscilloscope. Based on the output power requirements in both the fibers, the fiber pulling process can be stopped and flame can be turned off to end the fabrication process. Coupling ratio depends upon the measured output power from both the fibers. If the output power in both the fibers is exactly half the input power supplied to the coupler, then the coupling ratio is said to be 50:50.

Some of the disadvantages associated with flame-brush technique are the

contamination from the flame sources and uneven supply of flame heat due to disturbance caused by flow of air, which may affect the fabrication process.

CO_2 Laser

As per [76], a new method was reported to produce the optical directional couplers using CO_2 laser beam as a heating source in place a hydrogen flame. A beam of specific intensity is focused on the junction of the fibers using lens, which creates a thin hot spot in the coupler. This kind of setup provides major stability in fabricating a directional coupler as laser beam offers high precision in controlling the shape of coupling region. Some of the advantages using this technique are as follows:

- Free from contamination sources.
- Instant switch on and switch off of the Laser beam and
- Mobile laser source helps focusing beam at right spot on the coupler.

Some of disadvantages associated with using this method are as follows.

- Temperature produced by the beam varies over time during fabrication process.
- The input power to the laser source has to be controlled through out the process to build a successful coupler.

4.3 SCF-HCF Coupler

The SCF-HCF coupler is a 2 x 2 optical directional coupler and it is fabricated using hydrogen flame based process. We used SCF-28 as a primary fiber and polymicro capillary tubing (TSP320450) as a secondary fiber, which is the HCF. In order to expose the cladding of the primary fiber, the acrylate coating is removed using a fiber stripper. HCF contains a polyamide coating that protects it from abrasion by maintaining its strength and resistance. Some of the polyamide removal techniques are reported in the previous section. It is very important to make sure no scratches

present after removal of polyamide. Open flame technique was the effective way to remove the polyamide coating, where a general purpose lighter was used to burn off the coating followed with wiping of the burnt part with IPA to remove all the traces of burnt polyamide flakes. The SCF has a core of 5.3 μm in diameter and a cladding of 125 ± 1 μm. The diameter of the capillary tubing (HCF) inner core diameter is 320 ± 6 μm and its outer diameter is 435 ± 10 μm [77]. The coupler fabrication setup is as shown in Fig. 4.1. The coupler pulling station has two axially moving stages affixed with fiber clamps (Thor labs - T711-250), driven by stepper motors under the control of a graphical labview program. Both SCF and HCF fibers are twisted together near

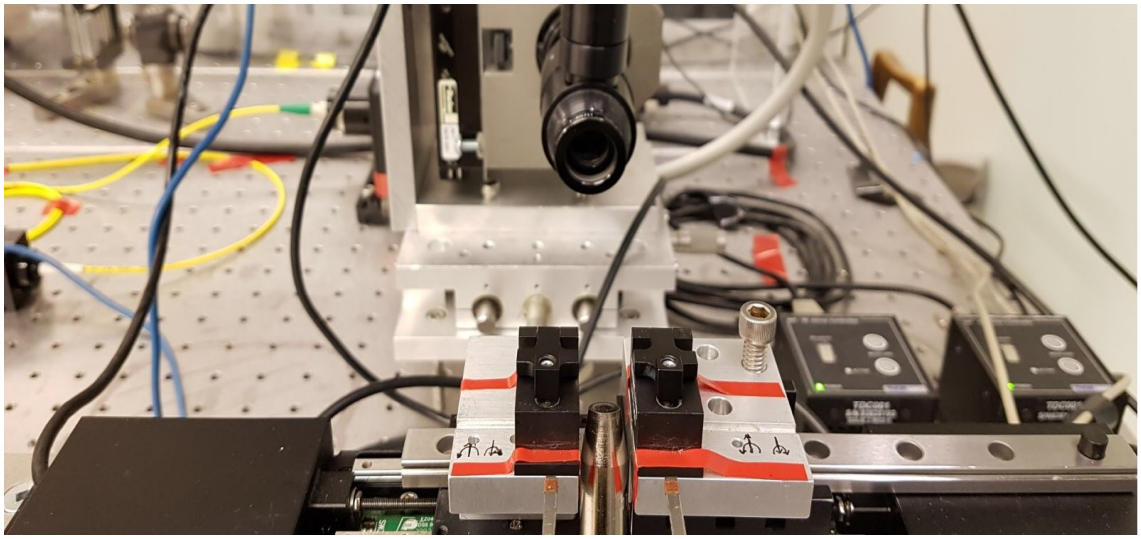

Figure 4.1: Fiber pulling setup with clamps on either side to hold the fibers and a hydrogen flame source underneath.

the coating free regions as shown in the microscopic Fig. 4.2 and the ends of the pair are placed in V-grooves of the fiber holding magnetic clamps on opposite sides and thus are held tightly. Hydrogen flame underneath points towards the twisted region of the pair, where the fibers are parallel to each other horizontally. During the fabrication, a laser source is connected to input of SCF and the ouput of SCF is connected to a optical power meter (new port 1830c). During the fabrication process, the hydrogen flame is switched on to heat up and melt the twisted fiber pair, forming a red hot region. The motors are turned on through thor labs APT labview software which pulls the movable stages in opposite directions resulting in pulling the fiber pair in opposite directions. The coupling takes place between the two fibers as per the coupling principle stated in chapter 2. The output of the power meter is recorded

through a data acquisition device (DAQ USB-6211), which is controlled by a custom built labview program. Also the program displays the change of transmission in SCF during the coupling process. The fabrication process is bound by the appropriate timelines and the process completes after the transmission from SCF couples twice into HCF, as displayed in the custom built labview program's waveform chart. The data recorded through labview program is shown in Fig. 4.3 as a plot of change of transmission flowing through SCF against the distance pulled.

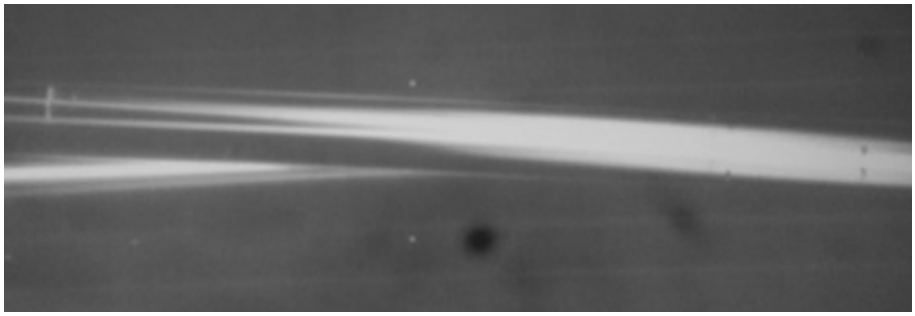

Figure 4.2: Microscopic figure of the twisted pair of SCF-HCF fibers held tightly on a fiber pulling stage.

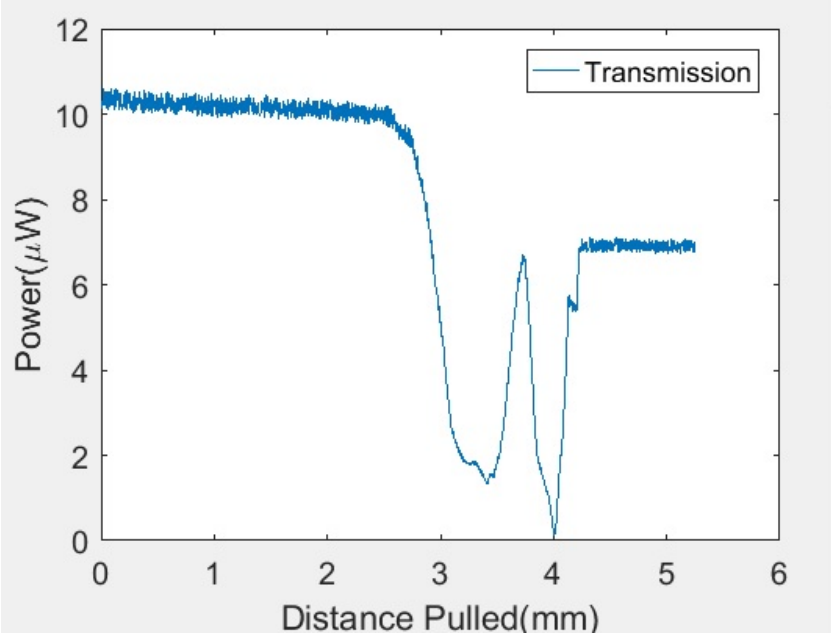

Figure 4.3: Periodic variation of power in SCF due to pulling of the fiber pair.

Chapter 5

Experiment and Results

5.1 Experiment

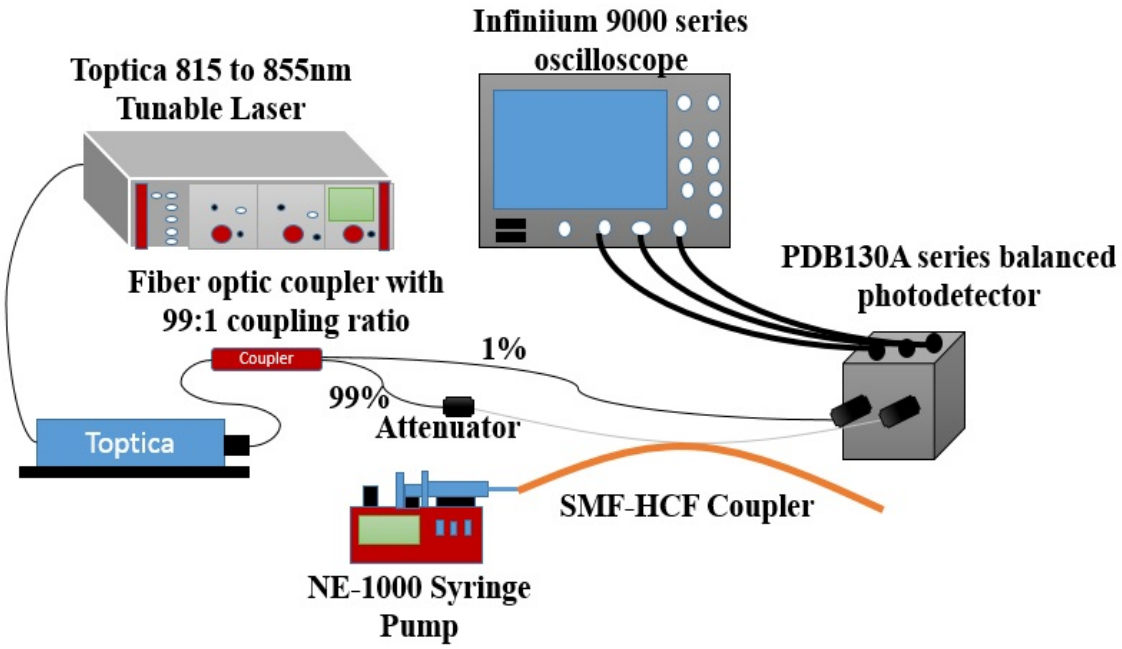

Figure 5.1: Schematic of experiment setup for refractive index measurement.

The sensing experiment setup is shown in Fig. 5.1. A laser (Toptica 815 to 855nm Tunable Laser) is connected to one of the input port of 2x2 fiber optic coupler with 99:1 coupling ratio. The 1% output branch is connected to a PDB100

series balanced photodetector. The 99% branch output port is connected to the SCF input port of our SCF-HCF coupler with a tunable attenuator in between. The SCF output port of our coupler further connects to the other input port of the balanced photodetector. The output voltage of the photodetector was recorded through infiniium 9000 series oscilloscope driven by a custom built labview program. A regular 10 ml syringe driven by an NE 1000 programmable syringe pump was connected to the input port of the HCF to deliver the liquid sample under test to the coupler.

The sample was delivered into the HCF at a rate of 0.1 mL/min by the syringe pump through a 21G needle, affixed to 10 ml syringe.

5.1.1 Sample Preparation

Glycerine/Glycerol/Glycerin is used in commercial and other scientific applications. It has unique physical properties such as stable, viscous, odorless, colorless and easily dissoluble in water. It is a product of soap family with a refractive index of 1.47.

Considering the physical and chemical properties of glycerol, it was used to prepare samples with different refractive indices. We prepared a total of six $1\,mL$ samples comprising of glycerol and DPBS in the percentage ratios of 0:100, 10:90, 20:80, 30:70, 40:60 and 50:50. We used a hand held pocket refractometer (Atago PAL-1) to determine the corresponding RI values for prepared samples.

The steps followed to obtain the RI values through the pocket refractometer include one time task of setting device display to zero by pressing down the zero key. During the measurement of samples, the refractometer was calibrated by measuring the refractive index of water after every round of RI measurement of the samples. The RI values measured to be 1.3316, 1.3675, 1.3767, 1.3830, 1.3963, 1.4039 with an uncertainty value of 0.0001 corresponding to 0%, 10%, 20%, 30%, 40% and 50% of glycerol in sample as shown in Fig. 5.2.

The uncertainty of 0.0001 was found by measuring the refractive index of distilled water sample for five consecutive times. The best estimate found from five trails was 1.3320 ± 0.0001.

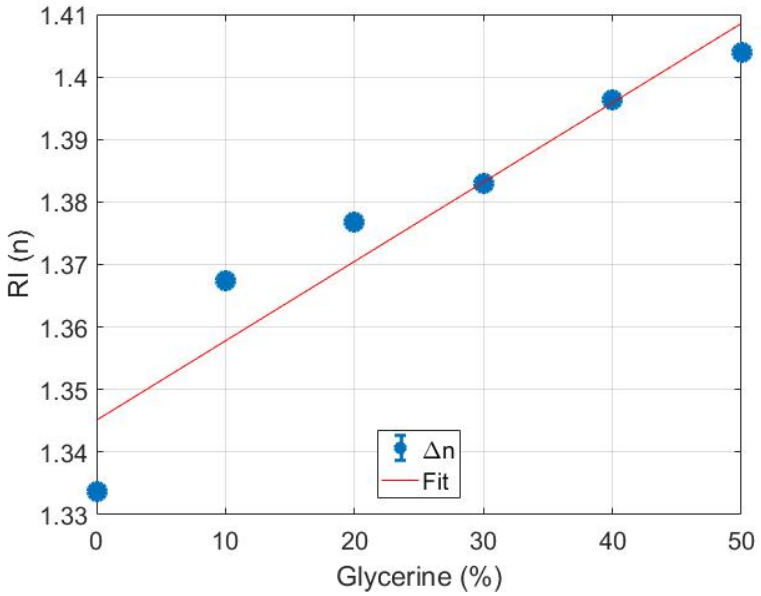

Figure 5.2: Refractive index (n) versus concentration (%) of glycerol in DPBS.

5.1.2 Results

In first set of experiments, different attenuation settings were used. Totally 4 sets of tests were performed using DPBS samples. The experiment steps include flowing of DPBS samples and air through HCF of SCF-HCF coupler in a sequence. The data was recorded during both sample and air injection. The transmission drop (ΔV) values corresponding to these tests were found to be 220.96, 238.53, 246.14, 217.03. Using these values, the resolution of our sensor can be measured. In the second set of experiments, initially buffered solution (DPBS) of RI(n)=1.331 was injected into HCF, the transmitted light at the output dropped suddenly as the water crosses the coupling section and the change in the voltage is recorded through custom built labview program. A least square fit of the transmission spectrum indicates that the transmitted signal dropped to 432.17 mV from 750.89 mV, yielding a voltage drop ΔV of 320.40 mV. Post recording the data, the DPBS was cleared from HCF by passing air through it. Later experiment trails included flowing of glycerol + DPBS samples and recording the corresponding ΔV values. HCF was cleaned with DPBS and air after every experiment conducted using DPBS + glycerol solution to ensure HCF is free from molecules of old samples. Fig. 5.4 shows a plot displaying all the ΔV values corresponding to change of glycerol percentage in the samples. Accurate

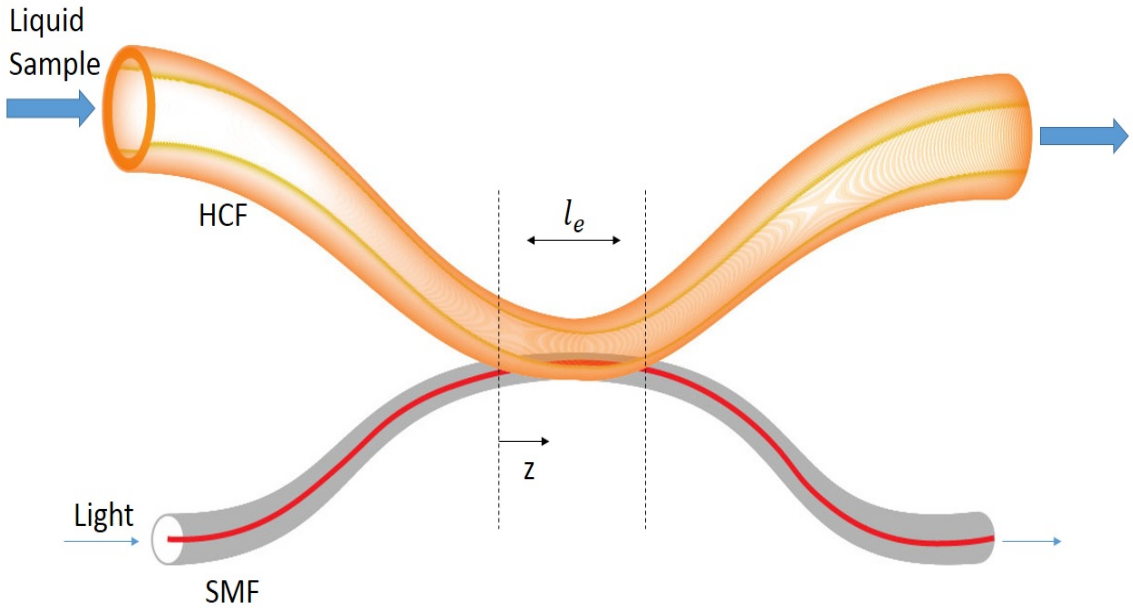

Figure 5.3: SCF-HCF coupler representing direction of flow of sample in HCF and light through SCF.

ΔV values were found through a custom fitting the transmission trace with a custom step function $(a*sign(x-x_0)+b)$, in which a, x_0 and b are the starting points used as coefficients in the step function. The amount of transmission drop recorded in second set of experiments as a function of change in refractive index of samples show a clear linear relation in Fig. 5.5.

The relationship between the amount of transmission drop and RI of glycerol is investigated through regression analysis, in which the change in voltage (ΔV) is a dependent variable and RI (n) of glycerol is an independent variable. Due to the linear nature of the relationship, we considered a straight line and it is the simplest linear regression curve i.e. $\Delta V = P(0) \times n + P(1)$. The plot shown in Fig. 5.5 also shows a residual or the error, which refers to the deviation between the linear curve and measured data. A minimum sensitivity of this sensor was estimated to be $4.02 \pm 0.50\, V/RIU$, through computing slope of linear curve. The precision value of 0.05 represents error associated with the slope of regression line and to calculate it we

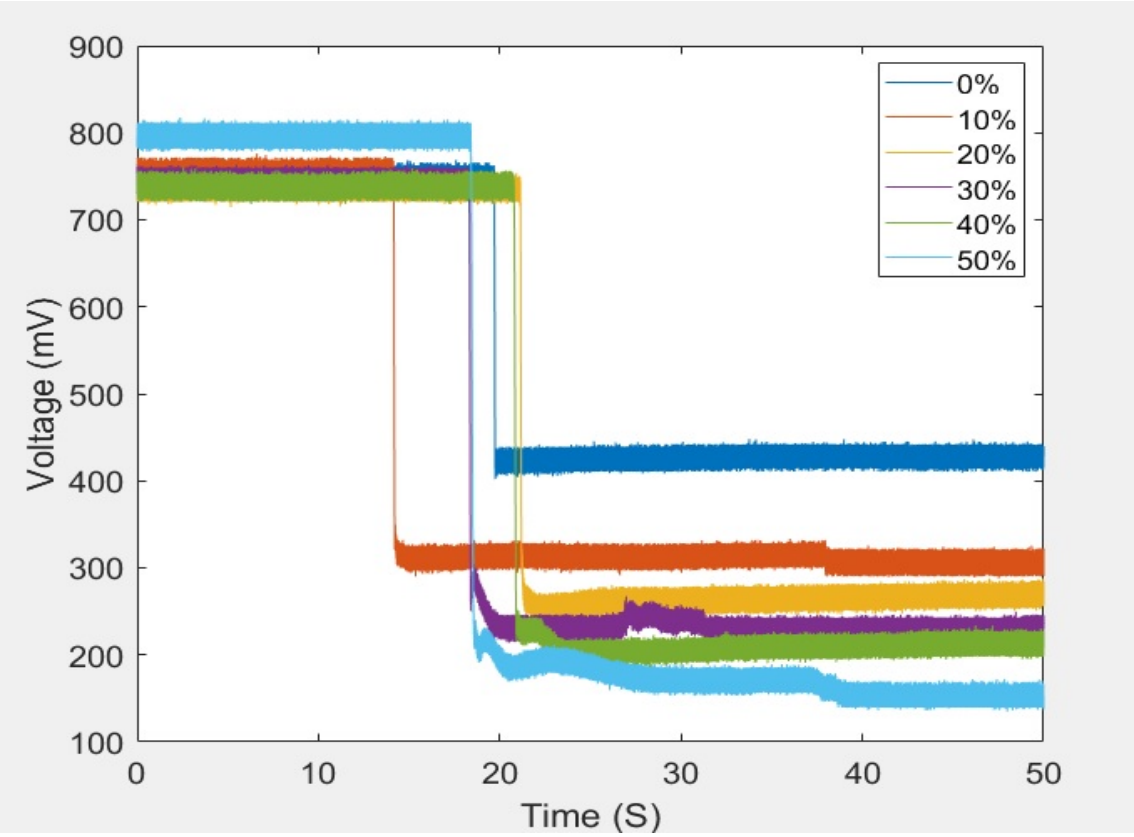

Figure 5.4: Plot showing the change in transmission voltage due to change of glycerol percentage in samples.

initially calculate the standard error of estimate or root mean square error (RMSE):

$$RMSE = \sqrt{\frac{\sum (y_i - \hat{y}_i)^2}{n-2}} = 27.92mV \tag{5.1}$$

in which, y_i and $\hat{y}_i$ are the predicted and measured responses. Since we are interested in estimating two parameters slope and intercept, so the degrees of freedom was opted as $n-2$.

Using RMSE, the error in slope was calculated to be:

$$\frac{RMSE}{\sqrt{\sum (x_i - \overline{x}_i)^2}} = 501.02\, mV/RIU \tag{5.2}$$

The coefficient of determination (R^2) shows the goodness of fit, i.e. if the value is 1, then the error between measured and predicted values is very minimal. A (R^2) value

of 0.9417 was calculated for our sensor, which shows that the measured values are very close to predicted values.

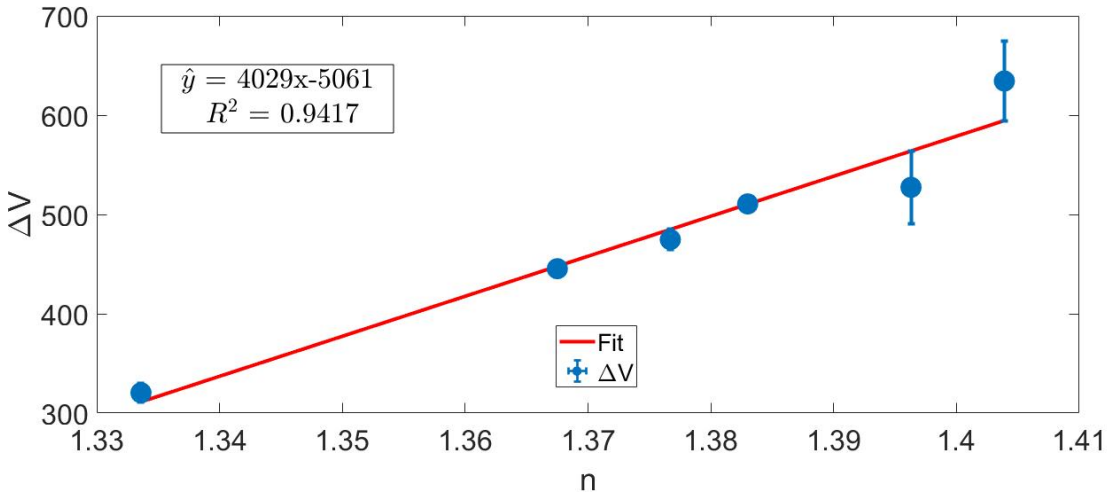

Figure 5.5: Output voltage drop in mV versus the refractive index of glycerol + DPBS samples.

Resolution refers to the smallest concentration or value that improves the confidence factor of measured quantity to 1 or the smallest input change that results in atleast 50% of output change. Through measuring the resolution, we can improve the accuracy of the measurement of refractive index. It can be calculated as:

$$SensorResolution = \frac{V_n}{S} \tag{5.3}$$

where V_n is the noise and S is the sensitivity of the sensor.

In order to calculate the noise, we calculated standard deviation values of ΔV obtained by repeated RI measurements of DPBS (blank) and the value was found to be 13.92 mV, using which the sensor resolution of $3.5 \times 10^{-3} RIU$ was calculated.

In SCF-HCF sensor system, there are different hardware components, such as oscilloscope, photodetector and laser system that are interconnected. The output signal obtained in the conducted experiment is directly dependent on the functioning of these components. In an ideal scenario, high sensor resolution can be obtained when there exists zero noise level in the measurement system. However, the photodetector and oscilloscope produce small amounts of noise that becomes dominant factor and affects the accuracy and precision of the measured quantities. Also the varia-

tions in the temperature of surrounding environment leads to change in the refractive index of the sample solution being tested. As a result of these factors, the sensor's resolution gets severely dented. The resolution of the sensor can be improved by overcoming such noise sources. Noise filters and usage of ultra-low noise photodetector can contribute towards reducing the overall noise present in the system, whereas the temperature fluctuations can be controlled through using a microheater that controls the temperature of the surrounding environment.

Due to the fact that multiple tests were performed, the side walls of the core of HCF remain wet and it affects the initial transmission before passing the sample and this in turn increases the overall value of standard deviation obtained from these tests.

5.2 Packaging SCF-HCF Coupler

The main objective behind packaging of our sensor is to make it sterilization free, such that the sample injected into the HCF shall not have any contact with the ambient environments. This also helps in avoiding sterilization process before recording the actual data. The package includes a microscopic glass slide where the sensor is placed and sealed.

5.2.1 Epoxy

UV-epoxy is a high performance adhesive used in wide number of applications which requires tight bonding. It posses many properties like high adhesion and low electrical conductivity, transparency etc. They are resistible to heat and chemicals. This adhesive is optically transparent and thus, it can be used with optical fiber and other capillary tubing.

Some of the disadvantages of using UV-epoxy are that the molecules in epoxy resin would flow with the sample contents and can increase the noise content in data recorded. The sample solution may get contaminated and can no longer be used. The other disadvantage is that, once the epoxy resin is dropped on a glass

surface, it can no longer be reused for packaging a new sensor.

5.2.2 PDMS

PDMS (polydimethylsiloxane) is a popular silicon based organic polymer and it belongs to the group of silicones. It has wide number of applications in medical, cosmetics and other related fields. In the field of optics, PDMS is used in fabricating fibers such as multi-mode optical fibers, looped, twisted and optical fiber couplers as demonstrated in [78].

PDMS also finds its applications in fabrication of other optical systems and microfluidic devices because of its versatile properties such as optically transparent, chemically inert and non-toxic. PDMS is an effective solution to fabricate optical components without affecting their performance. Once fabricated with PDMS, optical components can withstand high temperatures, show high transparency and minimal aging.

As given in [78], PDMS has a refractive index of 1.4118 at $25°C$ at 598 nm wavelength and 1.3997 at $25°C$ at 1554 nm. The absorption losses incurred in PDMS over the wavelength range of 400 to 1600 nm are lower than $5DBcm^{-1}$. This proves that PDMS is the ideal material for packaging our SCF-HCF coupler sensor. After building our sensor, a microscopic glass with attached micro heater (HT10K

Figure 5.6: Cured PDMS protecting the SCF-HCF coupler sensor.

Thor labs flexible resistive foil heater) was placed underneath it. The PDMS solvent is prepared by carefully mixing part a and part b solvent in the ratio of 10:1. The PDMS solvent is dropped carefully onto the sensor and glass surface underneath it.

The micro heater placed under the glass slide was supplied with sufficient voltage to increase the surface temperature to $70°C$ and it took approximately 10 minutes to cure the PDMS solvent. The sensor with cured PDMS is shown in Fig. 5.6 and further, the fiber ends are glued to the microscopic glass slide with epoxy.

Temperature sensing with SCF-HCF Coupler

As we know, a directional coupler has a specific coupling ratio that was achieved by periodic variation in the transmission at the time of pulling. This coupling ratio depends on lot of factors such as geometry of the coupler, refractive index of the material inside HCF and wavelength of light source. Based on this hypothesis, one such research was carried by [79], in which a 2X2 fused coupler was used as a temperature sensor.

In this report, we have already demonstrated the refractive index sensing by our SCF-HCF coupler. Further we tested our coupler to sense the change in temperature. As part of temperature sensing experiment, the packaged SCF-HCF coupler was placed on a hot plate that was operating at room temperature and the hollow core region of HCF was filled with DI water. The first experiment was carried out by increasing the temperature of hot plate at regular intervals until the temperature value reached to $80°C$. Every time the temperature was increased, the output power from the SCF increased. In the second experiment, we lowered the temperature at regular intervals until it reached to room temperature and in response to it, the output power from SCF reduced. During both the experiments, the output power from the SCF was recorded and was plotted against corresponding temperature as shown in Fig. 5.7.

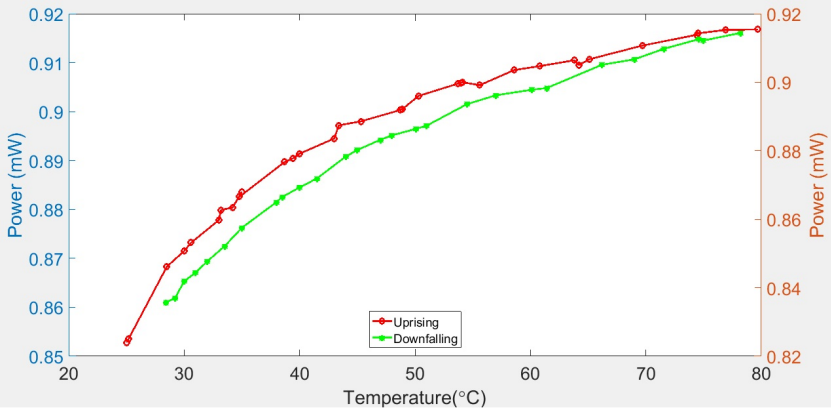

Figure 5.7: Simulated power in SCF as a function of temperature of the coupler filled with DI water.

Chapter 6

Conclusions and future work

6.1 Conclusions

We propose a novel approach using couple of fibers, which are HCF and SCF. These fibers are fused together to form an optical coupler so that light can be evanescently coupled between two fibers. The coupler can be fabricated using the flame brush method, that is using a hydrogen torch to taper the fibers while sketching them together. Here sample injection system with a laser source, a display mechanism and other supporting systems will be packaged as a permanent handheld application system. The SCF of the coupler is connected between the laser and the detector while the samples to be examined shall be injected by a syringe pump along the inner core of the HCF.

This sensing system is of low cost and offers great advantages, such as high repeatability, rapid sensing mechanism, free from contamination and onsite sterilization is not required. The residual sample inside the HCF can be cleaned by passing water. Thus, the sensing system can be reused for multiple tests. The sensor offers good sensitivity of $4.02 \pm 0.50\, V/RIU$ and a refractive index sensing resolution of $3.5 \times 10^{-3} RIU$ for refractive indices ranging from 1.331 ± 0.003 to 1.403 ± 0.003.

SCF-HCF coupler was also tested in sensing temperature and the experiment results were in good agreement with the theoretical understanding. The experiment

results clearly showed the rise and drop in the output power from SCF and it provides a strong evidence to say that our SCF-HCF coupler can also be used as a temperature sensor for the temperature ranging from $25°C$ to $80°C$.

The sensor was packaged carefully and the process followed was simple and very effective in improving the life span of the sensor. The packaging also protects the sensor from ambient environment and provides mechanical reliability.

6.2 Future work

The future work includes adding the improvements to make SCF-HCF sensor more compact, more sensitive and even low cost. The sample delivery system can be improved by integrating our sensor with microfluidic platform and as a result the volume of the sample solution can be greatly reduced. The SCF-HCF sensor can be converted to a compact handheld device by incorporating photodiode in place of expensive and huge sized laser system and mini photocells in place of big photodetectors.

Further research includes spectroscopic analysis, which can be introduced in this system. The light in the SCF fiber at the hot spot will interact with a biomolecule present in the HCF and it excites the Raman process from the sample. The Raman signal will further evanescently coupled back to the SCF fiber and captured by the spectrometer. By analyzing the received Raman spectrum, we can find the bio sample under investigation.

Appendix A

Derivation of Equations

A.1 Derivation steps of coupling coefficient

A.1.1 Formulation of Equation (2.50)

By substituting equation 2.43 into equation 2.48, we get:

$$\nabla \times (A(z)\vec{E}_{SCF}) + \nabla \times (B(z)\vec{E}_{HCF}) = -j\omega\mu_0(A(z)\vec{H}_{SCF} + B(z)\vec{H}_{HCF}) \quad \text{(A.1)}$$

By using below given vector identity from [73]

$$\nabla \times (A\vec{E}) = A(\nabla \times \vec{E}) + (\nabla A \times \vec{E}) = A(\nabla \times \vec{E}) + \frac{dA}{dz}(\hat{z} \times \vec{E}) \quad \text{(A.2)}$$

we get:

$$\begin{aligned} &A(z)\nabla \times \vec{E}_{SCF} + \frac{dA}{dz}(\hat{z} \times \vec{E}_{SCF}) + B(z)\nabla \times \vec{E}_{HCF} + \frac{dB}{dz}(\hat{z} \times \vec{E}_{HCF}) \\ &= -j\omega\mu_0 A(z)\vec{H}_{SCF} - j\omega\mu_0 B(z)\vec{H}_{HCF} \end{aligned} \quad \text{(A.3)}$$

By using maxwell's curl equations equations 2.13 and 2.14, we get:

$$\begin{aligned}&\frac{dA}{dz}(\hat{z}\times\vec{E}_{SCF})+\frac{dB}{dz}(\hat{z}\times\vec{E}_{HCF})\\&=A(z)[j\omega\mu_0\vec{H}_{SCF}-j\omega\mu_0\vec{H}_{SCF}]+B(z)[j\omega\mu_0\vec{H}_{HCF}-j\omega\mu_0\vec{H}_{HCF}]\end{aligned}\tag{A.4}$$

A.1.2 Formulation of Equation (2.51)

By substituting equation 2.42 into equation 2.49, we get:

$$\nabla \times (A(z)\vec{H}_{SCF}) + \nabla \times (B(z)\vec{H}_{HCF}) = j\omega\epsilon_0 n(A(z)\vec{E}_{SCF} + B(z)\vec{E}_{HCF}) \tag{A.5}$$

By making use of a vector identity [73] given in equation A.2, we get:

$$\begin{aligned} &A(z)(\nabla \times \vec{H}_{SCF}) + \frac{dA}{dz}(\hat{z} \times \vec{H}_{SCF}) + B(z)(\nabla \times \vec{H}_{HCF}) + \frac{dB}{dz}(\hat{z} \times \vec{H}_{HCF}) \\ &= j\omega\epsilon_0 nA(z)\vec{E}_{SCF} + j\omega\epsilon_0 nB(z)\vec{E}_{HCF} \end{aligned} \tag{A.6}$$

By using maxwell's curl equations 2.13 and 2.14, we get:

$$\begin{aligned} &A(z)j\omega\epsilon_0 n_{SCF}\vec{E}_{SCF} + \frac{dA}{dz}(\hat{z} \times \vec{H}_{SCF}) + B(z)j\omega\epsilon_0 n_{HCF}\vec{E}_{HCF} + \frac{dB}{dz}(\hat{z} \times \vec{H}_{HCF}) \\ &= j\omega\epsilon_0 nA(z)\vec{E}_{SCF} + j\omega\epsilon_0 nB(z)\vec{E}_{HCF} \end{aligned} \tag{A.7}$$

A.1.3 Formulation of Equation (2.54)

The expression to be integrated in equation 2.52 is expressed as

$$\vec{E}^*_{SCF} \cdot (LHS\, of\, eq.\, 2.51) - \vec{H}^*_{SCF} \cdot (LHS\, of\, eq.\, 2.50) \tag{A.8}$$

on expanding gives us with:

$$\begin{aligned} &= \vec{E}^*_{SCF} \cdot \left(\frac{dA}{dz}(\hat{z} \times \vec{H}_{SCF}) - j\omega\epsilon_0(n - n_{SCF})A\vec{E}_{SCF} + \frac{dB}{dz}(\hat{z} \times \vec{H}_{HCF}) \right. \\ &\left. - j\omega\epsilon_0(n - n_{HCF})B\vec{E}_{HCF} \right) - \vec{H}^*_{SCF} \cdot \left(\frac{dA}{dz}(\hat{z} \times \vec{E}_{SCF}) + \frac{dB}{dz}(\hat{z} \times \vec{E}_{HCF}) \right) \end{aligned} \tag{A.9}$$

$$\begin{aligned} &= \frac{dA}{dz}\left[\vec{E}^*_{SCF} \cdot (\hat{z} \times \vec{H}_{SCF}) - \vec{H}^*_{SCF} \cdot (\hat{z} \times \vec{E}_{SCF}) \right] + \frac{dB}{dz}\left[\vec{E}^*_{SCF} \cdot (\hat{z} \times \vec{H}_{HCF}) \right. \\ &\left. - \vec{H}^*_{SCF} \cdot (\hat{z} \times \vec{E}_{HCF}) \right] - j\omega\epsilon_0(n - n_{SCF})A\vec{E}_{SCF} \cdot \vec{E}^*_{SCF} - j\omega\epsilon_0(n - n_{HCF})B\vec{E}_{HCF} \cdot \vec{E}^*_{SCF} \end{aligned} \tag{A.10}$$

By using below vectorial formulas given in the appendix of [73]

$$\vec{E}^*_{SCF} \cdot (\hat{z} \times \vec{H}_{SCF}) = -\hat{z} \cdot (\vec{E}^*_{SCF} \times \vec{H}_{SCF}) \tag{A.11}$$

$$\vec{H}^*_{SCF} \cdot (\hat{z} \times \vec{E}_{SCF}) = \hat{z} \cdot (\vec{E}_{SCF} \times \vec{H}^*_{SCF}) \tag{A.12}$$

we get

$$\begin{aligned} &= -\frac{dA}{dz}\hat{z} \cdot [(\vec{E}^*_{SCF} \times \vec{H}_{SCF}) + (\vec{E}_{SCF} \times \vec{H}^*_{SCF})] - \frac{dB}{dz}\hat{z} \cdot [(\vec{E}^*_{SCF} \times \vec{H}_{HCF}) + (\vec{E}_{HCF} \times \vec{H}^*_{SCF})] \\ &- j\omega\epsilon_0(n - n_{SCF})A\vec{E}_{SCF} \cdot \vec{E}^*_{SCF} - j\omega\epsilon_0(n - n_{HCF})B\vec{E}_{HCF} \cdot \vec{E}^*_{SCF} \end{aligned} \tag{A.13}$$

A.1.4 Formulation of Equation (2.55)

The expression to be integrated in equation 2.53 is expressed as

$$= \vec{E}^*_{HCF} \cdot (LHS\, of\, eq.\, 2.51) - \vec{H}^*_{HCF} \cdot (LHS\, of\, eq.\, 2.50) \tag{A.14}$$

on expanding gives us with:

$$\begin{aligned} &= \vec{E}^*_{HCF} \cdot \left(\frac{dA}{dz}(\hat{z} \times \vec{H}_{SCF}) - j\omega\epsilon_0(n - n_{SCF})A\vec{E}_{SCF} + \frac{dB}{dz}(\hat{z} \times \vec{H}_{HCF}) - \right. \\ &\left. j\omega\epsilon_0(n - n_{HCF})B\vec{E}_{HCF} \right) - \vec{H}^*_{HCF} \cdot \left(\frac{dA}{dz}(\hat{z} \times \vec{E}_{SCF}) + \frac{dB}{dz}(\hat{z} \times \vec{E}_{HCF}) \right) \end{aligned} \tag{A.15}$$

$$\begin{aligned} &= \frac{dA}{dz}\left[\vec{E}^*_{HCF} \cdot (\hat{z} \times \vec{H}_{SCF}) - \vec{H}^*_{HCF} \cdot (\hat{z} \times \vec{E}_{SCF}) \right] + \frac{dB}{dz}\left[\vec{E}^*_{HCF} \cdot (\hat{z} \times \vec{H}_{HCF}) - \right. \\ &\left. \vec{H}^*_{HCF} \cdot (\hat{z} \times \vec{E}_{HCF}) \right] - j\omega\epsilon_0(n - n_{SCF})A\vec{E}_{SCF} \cdot \vec{E}^*_{HCF} - j\omega\epsilon_0(n - n_{HCF})B\vec{E}_{HCF} \cdot \vec{E}^*_{HCF} \end{aligned} \tag{A.16}$$

By using below vectorial formulas given in the appendix of [73]

$$\vec{E}^*_{HCF} \cdot (\hat{z} \times \vec{H}_{SCF}) = -\hat{z} \cdot (\vec{E}^*_{HCF} \times \vec{H}_{SCF}) \tag{A.17}$$

$$\vec{H}^*_{HCF} \cdot (\hat{z} \times \vec{E}_{SCF}) = \hat{z} \cdot (\vec{E}_{SCF} \times \vec{H}^*_{HCF}) \tag{A.18}$$

we get

$$\begin{aligned} &= -\frac{dA}{dz}\hat{z} \cdot [(\vec{E}^*_{HCF} \times \vec{H}_{SCF}) + (\vec{E}_{SCF} \times \vec{H}^*_{HCF})] - \frac{dB}{dz}\hat{z} \cdot [(\vec{E}^*_{HCF} \times \vec{H}_{HCF}) + (\vec{E}_{HCF} \times \vec{H}^*_{HCF})] \\ &- j\omega\epsilon_0(n - n_{SCF})A\vec{E}_{SCF} \cdot \vec{E}^*_{HCF} - j\omega\epsilon_0(n - n_{HCF})B\vec{E}_{HCF} \cdot \vec{E}^*_{HCF} \end{aligned} \tag{A.19}$$

Bibliography

[1] Lu, T. System and method for molecule sensing using evanescent light coupling approach., U.S. Patent 9921164 B2, Mar. 20, 2018.

[2] Farahani, H.; Wagiran, R.; Hamidon, M. N. Humidity sensors principle, mechanism, and fabrication technologies: a comprehensive review. *Sensors* **2014**, *14*, 7881-7939.

[3] Bhat, K. N.; Nayak, M. M. MEMS pressure sensors: an overview of challenges in technology and packaging. *Journal of ISSS* **2013**, *2*, 39-71.

[4] Catterall R.W. Chemical Sensors. *Oxford University Press* **1997**.

[5] Heijmans, J.A.C.; Cheng, L.K.; Wieringa, F.P. Optical fiber sensors for medical applications: Practical engineering considerations. *IFMBE Proceedings* **2009**, *22*, 23302334.

[6] Kerslake E. D. S.; Wilson, C. G. Pharmaceutical and biomedical applications of fiber optic biosensors based on infra red technology. *Elsevier* **1996**, *21*, 205-213.

[7] Kersey, A. D. A review of recent developments in fiber optic sensor technology. *Optical Fiber Technology* **1996**, *2*, 291-317.

[8] Senior, J. M. Optical fiber communications: Principles and practice. *Pearson Education.* **2009**.

[9] Poloso, T. Fibre bragg gratings optical sensing technology. *Smart Materials Bulletin* **2001**, *2001*, 7-10.

[10] Lee, B. Review of the present status of optical fiber sensors. *Optical Fiber Technology* **2003**, *9*, 57-79.

[11] Grattan, K. T. V.; Sun, T. Fiber optic sensor technology: an overview. *Sensors and Actuators* **2000**, *82*, 40-61.

[12] Pinto, A. M. R.; Lopez-Amo, M. Photonic crystal fibers for sensing applications. *Journal of Sensors* **2012**, *2012*, 21.

[13] Yeo, T. L.; Sun, T.; Grattan, K. T. V. Fiber-optic sensor technologies for humidity and moisture measurement. *Sensors and Actuators A: Physical* **2008**, *144*, 280-295.

[14] Yang, M.; Li, S.; Jiang, D. Review on optical fiber sensing technologies for industrial applications at the NEL-FOST. *HAL.*, **2014**, 361-368 .

[15] Agung, P. Evanescent waveguide sensors for biomedical applications. Delft University **2014**.

[16] Koohyar, F. Refractive index and its applications. *Thermodynamics and Catalysis* **2013**, *4*.

[17] Pereira, D. A.; Frazo, O.; Santos, J. L. Fibre Bragg grating sensing system for simultaneous measurement of salinity and temperature. *Opt. Eng.* **2004**, *43*, 299-304.

[18] Magwazaa, L. S.; Opara, U. L. Analytical methods for determination of sugars and sweetness of horticultural products-A review. *Elsevier* **2014**.

[19] Katsoulos, P. D.; Athanasiou, L.; Karatzia, M.; Giadinis, N.; Karatzias, H.; Boscos, C.; Polizopoulou, Z. S. Comparison of biuret and refractometry methods for the serum total proteins measurement in ruminants. *Veterinary Clinical Pathology* **Jul. 2017**.

[20] Sutton The refractometric determination of the total protein concentration in some animal species. *New Zealand veterinary journal* **1976**.

[21] Bianchetti, A.; Federico, A.; Vincent, S.; Subramanian, S.; Vollmer, F. Refractometry-based air pressure sensing using glass microspheres as high- Q whispering-gallery mode microresonators. *Optics Communications.* **2017**.

[22] Guider, R.; Gandolfi, D.; Chalyan, T.; Pasquardini, L.; Samusenko, A.; Pederzolli, C.; Pucker, G.; Paves, L. Sensitivity and limit of detection of biosensors based on ring resonators. *Sensing and Bio-Sensing Research.* **2015**, *6*, 99-102.

[23] Fei Xing; Gui-Xian Meng; Qian Zhang; Lei-Ting Pan; Peng Wang; Zhi-Bo Liu; Wen-Shuai Jiang; Yongsheng Chen; Jian-Guo Tian Ultrasensitive flow sensing of a single cell using graphene-based optical sensors. *Nano Letters.* **2014**, *14*, 3563-3569.

[24] Alankar, S; Gupta, V. B. Methods for the determination of limit of detection and limit of quantitation of the analytical methods. *Chronicles of young scientists.* **2011**, *2*, 21-25.

[25] Rees, N. D. ; James, S. W.; Tatam, R. P.; Ashwell, G. J. Optical fiber long-period gratings with Langmuir blodgett thin-film overlays. *Opt. Lett.* **2002**, *27*, 686-688.

[26] Rindorf, L.; Bang, O. Highly sensitive refractometer with a photonic-crystal-fiber long-period grating, *Opt. Lett.* **2008**, *33*, 563-565.

[27] Wu, D. K. C.; Kuhlmey, B. T.; Eggleton, B. J. Ultrasensitive photonic crystal fiber refractive index sensor. *Opt. Lett.* **2009**, *34*, 322324.

[28] Liedberg, B.; Nylander, C. Biosensing with surface plasmon resonance-How it all started. *biosensors and bioelectrics*, **1995**.

[29] Mishra, S. K.; Zou, B.; Chiang, K. S. Surface-plasmon-resonance refractive-index sensor with cu-coated polymer waveguide. *IEEE photonics technology letters* **2016**, *28*, 1835-1838.

[30] Liu, Q.; Chiang, K. S. Refractive-index sensor based on long-range surface plasmon mode excitation with long-period waveguide grating. *Opt. Exp.* **2009**, *17*, 79337942.

[31] Homola, J.; tyrok, J.; Skalsk, M.; Hradilov, J.; Kolov, P. A surface plasmon resonance based integrated optical sensor. *Sensors and Actuators B: Chemical* **1997**, *39*, 286 - 290.

[32] Villatoro, J.; Monzn-Hernndez, D.; Meja, E. Fabrication and modeling of uniform-waist single-mode tapered optical fiber sensors. *Appl. Opt.* **2003**, *42*, 2278-2283.

[33] Homola, J. Present and future of surface plasmon resonance biosensors. *Anal. Bioanal. Chem.* **2003**, *377*, 528-539.

[34] Hill, K. O.; Meltz, G. Fiber bragg grating technology fundamentals and overview. *Journal of lightwave technology.* **1997**, *15*, 1263-1276.

[35] Chen, J.; Liu, B.; Zhang, H. Review of fiber bragg grating sensor technology. *Front. Optoelectron. China* **2011**, *4*, 204212.

[36] Frazo, O.; Martynkien, T.; Baptista, J. M.; Santos, J. L.; Urbanczyk, W.; Wojcik, J. Optical refractometer based on a birefringent bragg grating written in an H-shaped fiber. *Opt. Lett.* **2009**, *34*, 76-78.

[37] Tsigaridas, G.; Polyzos, D.; Ioannou, A.; Fakis, M.; Persephonis, P. Theoretical and experimental study of refractive index sensors based on etched fiber Bragg gratings. *Sensors and Actuators A: Physical.* **2014**, *209*, 9-15.

[38] Zhou, K.; Chen, X.; Zhang, L.; Bennion, I. High-sensitivity optical chemsensor based on etched D-fibre bragg gratings. *Electronics Letters* **2004**, *40*, 232-234.

[39] Renner R., Kehrli M., Lthy W.; Weber H. P. Manufacturing of a D-shaped fiber. *Laser Physics* **2003**, *13*, 232-3.

[40] Zaatar, Y.; Zaouk, D.; Bechara, J.; Khoury, A.; Llinaress, C.; Charles, J. P. Fabrication and characterization of an evanescent wave fiber optic sensor for air pollution control. *Materials Science and Engineering: B* **2000**, *74*, 296-298.

[41] Asseh, A.; Sandgren, S.; Ahlfeldt, H.; Sahlgren, B.; Stubbe, R.; Edwall, G. Fiber optical bragg grating refractometer. *Fiber and Integrated Optics* **1998**, *17*, 51-62.

[42] Liang, W.; and Huang, Y.; Xu, Y.; Lee, R. K.; Yariv, A. Highly sensitive fiber bragg grating refractive index sensors. *Applied Physics Letters* **2005**, *86*, 151122.

[43] Meltz, G.; Hewlett, S. J.; Love, J. D. Fiber grating evanescent-wave sensors. *SPIE Proceedings.* **1996**, *2836*, 342.

[44] Tazawaa, H.; Kanie, T.; Katayama, M. Fiber-optic coupler based refractive index sensor and its application to biosensing. *Meas. Sci. Technol.* **2007**, *91*, 113901.

[45] James, S. W.; Tatam, R. P. Optical fibre long-period grating sensors: characteristics and application. *Meas. Sci. Technol.* **2003**, *14*, R49R61.

[46] Bal, H. K. Optical fiber refractive Index, voltage and strain sensors: fabrication and applications. doctoral, Victoria University. Faculty of Health, Engineering and Science, Victoria University, Australia, **2011**.

[47] Nidhi, R. S. K.; Kapur, P. Theoretical and experimental study of long-period grating refractive index sensor. *Fiber and Integrated Optics* **2014**, *33*, 37-46.

[48] Bhatia, V. Optical fiber long-period grating sensors. *Optics Letters.* **1996**, *21*, 692-694.

[49] Del Villar, I.; Achaerandio, M.; Matas, I. R.; Arregui, F. J. Optimization of sensitivity in long period fiber gratings with overlay deposition. *Opt. Express.* **2005**, *13*, 5668.

[50] Rego, G. M.; Santos, J. L.; Salgado, H. M. Refractive index measurement with long-period gratings arc-induced in pure-silica-core fibres. *Opt. Commun.* **2006**, *259*, 598602.

[51] Du, C.; Wang, Q.; Wang, X.; Zhao, Y.; Hu, H. High sensitivity internal refractive index sensor based on a photonic crystal fiber long period grating. *Instrumentation Science and Technology.* **2016**.

[52] Buczynski, R. Photonic crystal fibers. *Acta Physica Polonica Series a*, **2004**.

[53] Qu, H.; Skorobogatiy, M. Liquid-core low-refractive-index-contrast Bragg fiber sensor. *Applied Physics Letters* **2011**, *98*, 201114.

[54] Darran, K. C. W.; Kwang, J. L.; Vincent, P.; Boris, T. K. Performance of refractive index sensors based on directional couplers in photonic crystal fibers. *Journal of lightwave technology.* **1986**, *31*, 3500-3510.

[55] Zheng, K.; Shang, L. High-Linearity refractive index sensor based on analyte-filled defect hollow core bragg fiber. *IEEE photonics technology letters* **2017**, *29*, 1391-1394.

[56] Zhao, Y.; Li, X. G.; Cai, L.; Zhang, Y. N. Measurement of RI and temperature using composite interferometer with hollow-core fiber and photonic crystal fiber. *IEEE transactions on instrumentation and measurement* **2016**, *65*, 2631-2635.

[57] Donlagic, D.; Cibula, E. All-fiber high-sensitivity pressure sensor with SiO_2 diaphragm. *Optics Express* **2005**, *30*, 2071-2073.

[58] Choi H. Y.; Mudhana G.; Park K. S.; Paek U. C.; Lee B. H. Cross-talk free and ultra-compact fiber optic sensor for simultaneous measurement of temperature and refractive index. *Optics Express* **2010**, *18*, 141-149.

[59] Ozel, B.; Nett, R.; Weigel, T.; Schweiger, G.; Ostendorf, A. Temperature sensing by using whispering gallery modes with hollow core fibers. *Measurement Science and Technology* **2010**, *21*, 1-5.

[60] Zhao, Y.; Tong, R. J.; Chen, M. Q.; Xia, F. Fluorescence temperature sensor based on gqds solution encapsulated in hollow core fiber. *IEEE photonics technology letters* **2017**, *29*, 1544-1547.

[61] Chen, J. C.; Ho, C. W.; Wang, J. S. Optical Fiber coupler with a hollow core fiber for magnetic fluid detection. *Lightwave Technology* **2012**, *34*, 5220-5225.

[62] Luff, B. J.; Harris, R. D.; Wilkinson, J. S.; Wilson, R.; Schiffrin, D. J. Integrated-optical directional coupler biosensor. *Optics Letters* **1996**, *21*, 618-620.

[63] Shin, W.; Choi, S.; Oh, K. All-fiber wavelength- and mode-selective coupler for optical interconnections. *Optical Society of America* **2002**, *27*.

[64] Liu, J.; Cheng, T. H.; Yeo, Y. K.; Wang, Y.; Xu, Z.; Wang, D. Fused biconical tapered technique based light beam coupling between a single mode fiber and a high nonlinearly photonic crystal fiber. *Optical Society of America. 2009*.

[65] Yokota, H.; Yashima, H.; Imai, Y.; Yutaka Sasaki, Y. Coupling characteristics of fused optical fiber coupler formed with Single-mode fiber and photonic crystal fiber having air hole collapsed taper. *Advances in OptoElectronics* **2016**, -8.

[66] Kim, K. T.; Kim, H. K.; Hwangbo, S.; Choi, S.; Lee, H. B.; Kyunghwan Oh, K. Characterization of evanescent wave coupling in side-polished hollow optical fiber and its application as a broadband coupler. *Optics Communications* **2005**, 145-151.

[67] Rahnavardy, K.; Arya, V.; Wang, A.; Weiss, J. M. Investigation and application of the frustrated-total-internal-reflection phenomenon in optical fibers. *Appl. Opt.* **1997**, *36*, 21832187.

[68] OKeeffe, D. G. Development of fiber optic evanescent-wave fluorescent-based sensors. doctoral, Dublin City University. School of Physical Sciences, **1995**.

[69] Harlepp, S.; Robert, J.; Darnton, N.; Chatenay, D. Subnanometric measurements of evanescent wave penetration depth using total internal reflection microscopy combined with fluorescent correlation spectroscopy. *Applied Physics Letters* **2004**, *85*, 3917-3919.

[70] Daendliker, R. The concept of modes in optics and photonics. *Proc. SPIE 3831, Sixth International Conference on Education and Training in Optics and Photonics.* **2000**, *3831*, 193-198.

[71] Kawano, K.; Kitoh, T. Introduction to optical waveguide analysis. *John Wiiley and Sons, Inc.* **2001**.

[72] Ghatak, A.; Thyagarajan, K. Introduction to fiber optics. *Cambridge university press* **1997**.

[73] Okamoto, K. Fundamentals of optical waveguides. *New York, NY, USA: Academic Press* **2005**.

[74] Ivanov, S. Theoretical and quantum mechanics. *Springer* **2006**.

[75] Macomber, J.; Lui, P.; Acuna, R. Polymicro technologies fused silica capillary tubing: selecting a cutting method. *LCGC, The Application Notebook* **2009**.

[76] Dimmick, T. E.; Kakarantzas, G.; Birks, T. A.; Russell, P. St. J. Carbon dioxide laser fabrication of fused-fiber couplers and tapers *Applied Optics* **1999** *38*, 6845-6848.

[77] Polymicro Technologies Polyimide coated fused silica capillary tubing. TSP320450 datasheet. **2016**.

[78] Martincek, I.; Pudis, D.; Chalupova, M. Technology for the preparation of pdms optical fibers and some fiber structures. *IEEE Photonics technology letters* **2014**, *26*, 1446-1449.

[79] Kim, K.T.; Park, K.H. Fiber-optic temperature sensor based on single mode fused fiber coupler. *Journal of the Optical Society of Korea* **2008**, *12*, 152-156.